iScience

CellPress

Article

Synergizing Photo-Thermal H_2 and Photovoltaics into a Concentrated Sunlight Use

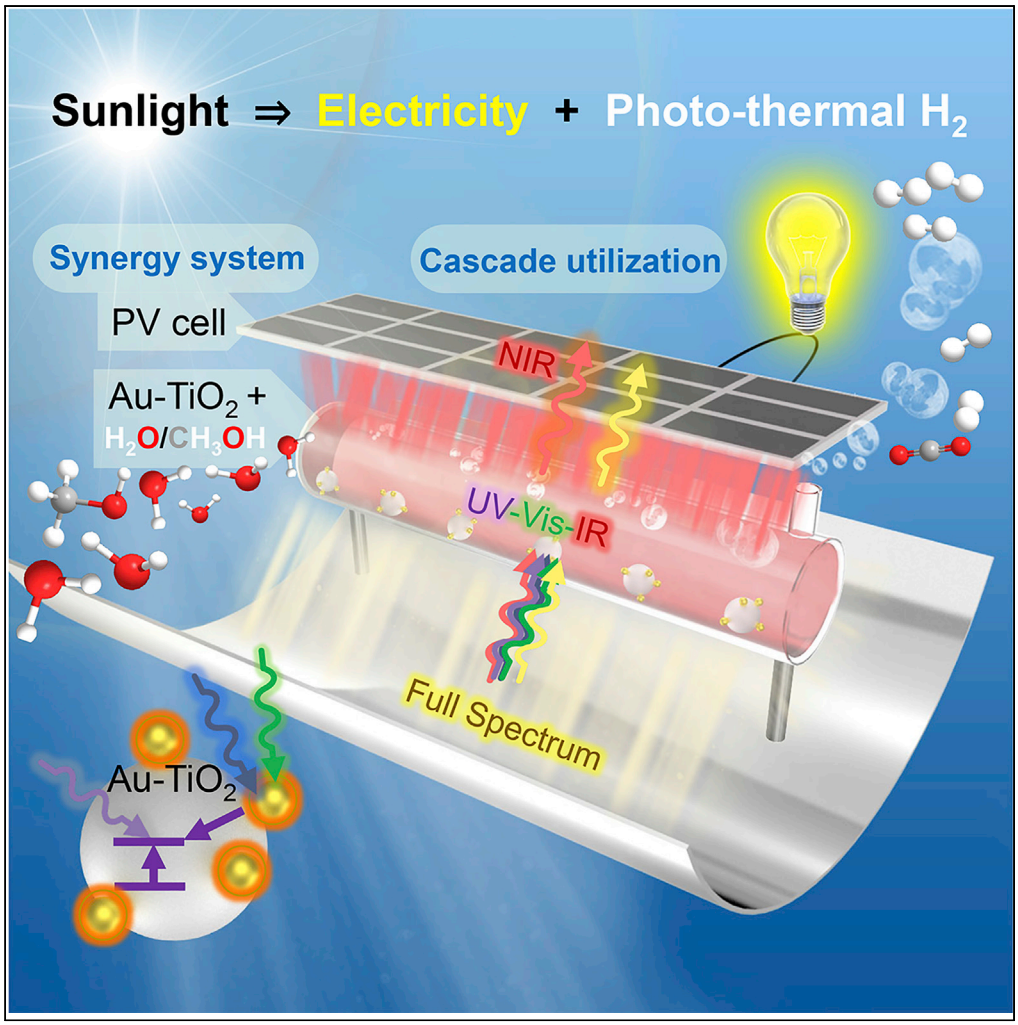

Sanli Tang, Xueli Xing, Wei Yu, ..., Yangfan Xu, Hui Hong, Hongguang Jin

honghui@iet.cn

HIGHLIGHTS

An integration of both photothermal H_2 and PV was proposed at full solar spectrum

Absorbed UV-vis and IR generate H_2 faster than reported full-spectrum catalysis

Transmitted Vis and near-IR bands retain the high efficiency of commercial PV cells

A novel device was designed with experimental overall efficiency of 4.2% at 12 suns

Tang et al., iScience *23*, 101012
April 24, 2020
https://doi.org/10.1016/j.isci.2020.101012

iScience

CellPress

Article

Synergizing Photo-Thermal H_2 and Photovoltaics into a Concentrated Sunlight Use

Sanli Tang,[1,2,6] Xueli Xing,[1,2] Wei Yu,[3] Jie Sun,[4] Yimin Xuan,[5] Lu Wang,[6] Yangfan Xu,[6] Hui Hong,[1,2,7,*] and Hongguang Jin[1,2]

SUMMARY

Solar hydrogen and electricity are promising high energy-density renewable sources. Although photochemistry or photovoltaics are attractive routes, special challenge arises in sunlight conversion efficiency. To improve efficiency, various semiconductor materials have been proposed with selective sunlight absorption. Here, we reported a hybrid system synergizing photo-thermochemical hydrogen and photovoltaics, harvesting full-spectrum sunlight in a cascade manner. A simple suspension of Au-TiO_2 in water/methanol serves as a spectrum selector, absorbing ultraviolet-visible and infrared energy for rapid photo-thermochemical hydrogen production. The transmitted visible and near-infrared energy fits the photovoltaic bandgap and retains the high efficiency of a commercial photovoltaic cell under different solar concentration values. The experimental design achieved an overall efficiency of 4.2% under 12 suns solar concentration. Furthermore, the results demonstrated a reduced energy loss in full-spectrum energy conversion into hydrogen and electricity. Such simple integration of photo-thermochemical hydrogen and photovoltaics would create a pathway toward cascading use of sunlight energy.

INTRODUCTION

Generating clean and storable hydrogen from sunlight has been pursued as a fundamental technology for the future of humanity (IEA, 2019). The past several decades have seen a wide array of research on fundamental and applied sciences and engineering toward an efficient and economic sunlight-hydrogen energy conversion process. The concept of "one-pot" solar-hydrogen conversion process is highlighted by using a single solar reactor, ensuring outstanding feasibility and scalability (Ozin, 2017). By its nature, the sunlight energy source includes the broad UV, visible, and infrared bands, generating both electrical and thermal effects for hydrogen generation. By directly using the driving forces, solar photochemical and solar thermochemical conversions emerge for producing "one-pot" solar hydrogen (Tavasoli and Ozin, 2018).

In the photochemical process, the photo-excited charge carriers as a driving force is naturally high-grade electrical energy. Typically, the photocatalytic water splitting is a process from charge carriers to chemical energy in hydrogen, with a leading solar-to-hydrogen efficiency of 1.1% (Wang et al., 2016). Although it is a high-quality electrical-chemical process, the photocatalysis usually has a low efficiency. Thermodynamically, one reason may be the photochemically used high-grade UV band only covers 5% in full spectrum energy, losing most of the Vis-IR band. On the other hand, the high quality of photon energy is severely damaged associating with the irreversibility, because the sunlight has variable spectral energy quantity and quality and is hard to fit with a single bandgap. At the full-spectrum scale, efforts have been made to derive more charge carriers with lower-energy grade from broadband sunlight photons at longer wavelength (Cao et al., 2019; Yang et al., 2019). To reinforce the energy grade, the broadband water splitting requires the assistance of the Z-scheme or sacrificial reagents (Liang et al., 2018; Qi et al., 2018; Liu et al., 2018; Fang et al., 2019). However, a previous study still revealed a dilemma between the energy quantity and quality: the most popular $BiVO_4$ has a recombination of 50%–70% in the UV band and >80% in the Vis band (Zhao et al., 2014). The recombined charge carrier then dissipated as low-temperature heat, causing irreversibility. Toward the 5%–10% solar-to-hydrogen efficiency target for industrial scalable solar photochemistry (Pinaud et al., 2013), the breakthrough is needed on improving both the quality and quantity of photocatalytic utilization. One is to match the semiconductor bandgap to full spectrum photon energy. Then, the gap in energy grade can be minimized between the energy donor and acceptor, reducing the irreversible energy loss.

[1]University of Chinese Academy of Sciences, Beijing 100049, China

[2]Institute of Engineering Thermophysics, Chinese Academy of Sciences, Beijing 100190, China

[3]School of Environmental and Materials Engineering, College of Engineering, Shanghai Polytechnic University, Shanghai 201209, China

[4]School of Chemical Engineering and Technology, Xi'an Jiaotong University, Xi'an, Shaanxi 710049, China

[5]School of Energy and Power Engineering, Nanjing University of Aeronautics and Astronautics, Nanjing 210016, China

[6]Solar Fuels Group, Department of Chemistry, University of Toronto, 80 St. George Street, Toronto M5S 3H6, Canada

[7]Lead Contact

*Correspondence: honghui@iet.cn

https://doi.org/10.1016/j.isci.2020.101012

Another is to properly utilize the long-wavelength sunlight with photon energy lower than bandgap, assisting the H_2 production.

Originating from the needs of photochemical conversion, the photo-thermocatalytic conversion is proposed by synergizing the photo-thermal driving forces (Ghoussoub et al., 2019). Ozin et al. demonstrated that a nano-heater under sunlight irradiation can produce localized heat to improve the surface reaction rate (Jia et al., 2016). The localized heat was also found to assist the low-grade photons in bandgap excitation (Li et al., 2019b). The Vis and IR sunlight can generate localized heat in processes like recombination, surface plasmonic resonance (SPR), or even the reactant molecular absorption of sunlight. Through controlling such processes, the low-grade Vis and IR photons can join the production of photo-thermal H_2 instead of being dissipated as low-temperature heat. In the photochemical component of photo-thermocatalysis, the UV-vis-generated charge carriers may provide a bypass circumventing the thermal activation barrier, reducing the activation energy (Ghoussoub et al., 2019; Li et al., 2019c). In addition, the consumption of photo-generated holes also benefits from an elevated temperature, often induced by localized heat from the IR band (Fang et al., 2019). Then the photochemical process provides more photo-excited electrons, accelerating the surface H_2 evolution. The photo-thermocatalysis is no longer an individual photochemical or thermochemical process (Tang et al., 2017) but a photo-thermal integrated systematic utilization at a broadband solar spectrum scale.

Besides the photo-thermocatalytic conversion, there is another method for photo-thermal integrated systems that use spectral splitting. Typically, a band-pass spectrum splitter transmits the near infrared (NIR) band for photovoltaic (PV) electricity generation, while absorbing the UV-vis-IR band for solar thermochemistry or solar heat generation (Tang et al., 2018; Weinstein et al., 2018). In recent reports, even the PV itself can become a spectrum selector transmitting below-bandgap photons for solar heat (Xu et al., 2020). Such spectral splitting methods matched the photovoltaic (PV) conversion with the Vis-IR band, where the PV is more efficient than with full-spectrum, thus improving the overall efficiency. This inspires us to a potential synergy of PV and solar photo-thermochemistry. A not only spectral selective but photo-thermal catalytic solution can enable a synergy system of solar H_2 and PV electricity, both at their most desirable solar spectrum band.

Herein, we provide a solar energy system co-generating H_2 and electricity in a cascade-like conversion of the concentrated sunlight. Matching the energy grade between the solar spectrum and the conversions, the system uses not only the UV-vis/IR band for photo-thermal H_2 but also the Vis and near-infrared (NIR) band for PV electricity. We designed an experimental device to identify the key problems in the cascade-like conversion of the concentrated sunlight. A simple Au-TiO_2 suspended reaction solution is designed like a spectral selector, absorbing the UV-IR while transmitting the Vis-NIR bands. Under an input sunlight intensity as high as 15 suns, we found that the H_2 productivity using the UV-vis and IR narrow band gained a 30%–40% improvement to full-spectrum absorptive sophisticated photo-thermocatalysis. The transmitted visible and near-infrared energy coincided with the photovoltaic bandgap and maintained the high efficiency of a commercial photovoltaic cell under different solar concentration values. The experimental design achieved an overall efficiency of 4.2% for a solar concentration of 12 suns. Further analysis on energy flow enlightened that through selectively absorbing the useful photons, it is easier to separate charge carriers.

RESULTS AND DISCUSSION

Synergizing Concentrated Photo-Thermal Hydrogen and Photovoltaics

The research in photocatalysis has provided various means to expand the spectrum absorption, such as using compound bandgap semiconductors with a core-shell, anchored, or a multilayer structure (Liu et al., 2017a). In the present work, we selected a simple Au-TiO_2 catalyst and obtained spectral selectivity along with absorptivity. The hybrid system, schematically shown in Figure 1, proposes a cascade pathway converting the concentrated sunlight into photo-thermal H_2 and PV electricity. A parabolic trough solar collector concentrates the sunlight to 15 suns. In the upstream photo-thermal H_2 process, the concentrated sunlight enters the Au-TiO_2 mixed methanol/water reaction solution. The reaction solution functions as a spectrum "selector," absorbing the UV-vis/IR band while transmitting the Vis-NIR band. Through such a selector, the energy of UV-vis/IR band drives the photo-thermocatalysis and is converted into the chemical energy in H_2. In the downstream photovoltaic process, the integrated PV cell receives the Vis-NIR band transmitted out of the reaction solution. In contrast, an individual PV is prone to relaxation or carrier

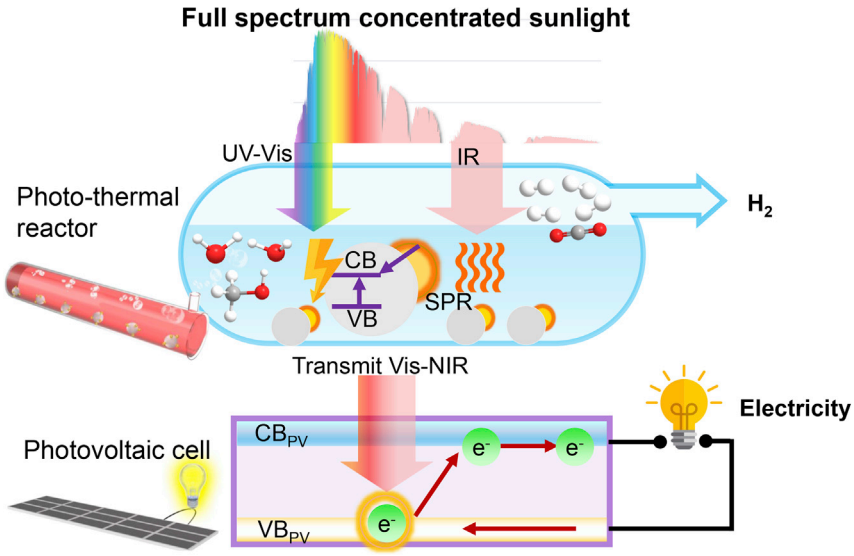

Figure 1. Synergizing Concentrated Photo-Thermal Hydrogen and Photovoltaics

Schematic of the concentrated solar system synergizing photo-thermal H_2 and PV electricity in a cascade pathway.

recombination in the UV-vis/IR band, generating waste heat. Based on the second law of thermodynamics, the waste heat generation is the destruction of the potential for conversion into electricity or chemical energy. By selecting the UV-vis/IR for upstream and transmitting Vis-NIR for downstream, this work maintains the energy grade of the sunlight converted into chemical energy and electricity.

Selective Absorption for Photo-Thermal Hydrogen

Figure 2 shows the experimental apparatus for the cascading production of photo-thermal H_2 and electricity from full-spectrum sunlight (more details in Figures S10 and S11). We assembled a convex lens on a 300 W xenon lamp and achieved a concentrated sunlight input of 15 suns. The intensity was measured at the same location and orientation of the surface of the reaction solution (Li et al., 2019a). For photo-thermocatalysis, loaded Au was controlled at an average d = 15 nm (Figures S1 and S12) to acquire an absorbing peak at 400–700 nm Vis band. The morphology remained stable after 40 h of experiments (Figures S1 and S2). By dispersing Au-TiO_2 in 10% vol methanol, a near-homogeneous volumetric liquid absorber was obtained with UV-vis/IR absorption and Vis-NIR transmittance. Then, an over 95% transmittivity quartz reactor was adopted to contain the liquid absorber to minimize the optical losses. The reactor cap was blurred by the reactant steam; thus, we pasted a defogger heating the cap at 110°C to prevent blurring. There also existed outward scattering around the side of the reactor; therefore, an over 95% reflective film was used to recollect the scattering. Consequently, most of the scattered and unabsorbed sunlight was transmitted out of the reactor bottom. The total transmitted sunlight was measured using a spectrometer as 700–1,100 nm wavelength in the Vis-NIR band (Figure S3). Furthermore, the transmitted NIR coincided with the 1.2- to 1.3-eV bandgap of mono-crystalline silicon, driving the commercial PV cell to obtain electricity.

Figure 3 shows the photo-thermocatalysis performance using UV-vis/IR spectrum under concentrated sunlight of C = 1–15. The H_2 generation rate increased in proportion to the increasing solar concentration ratio, and the highest rate was 750–1,300 mL g_{cat}^{-1} h^{-1} at C = 9–15 (see Video S1). Even at C = 7, we used the UV-vis/IR band to generate H_2 at 435 mL h^{-1} g^{-1}. The results indicate that the UV-vis/IR narrow band is sufficient for H_2 generation owing to the high UV-vis energy grade (>2 eV) for charge carrier excitation and an elevated IR phonon energy grade by photo-thermal synergy. Using broadband absorptive catalysts such as SiO_2/Ag@TiO_2 or Pt-TiO_2, previous studies also reported photo-thermal H_2 generation rates of <460 mL h^{-1} g^{-1} at C = 2–7 with the same sacrificial reagent (for detailed data see Table S1) (Chiarello et al., 2010, 2014; Elbanna et al., 2017; Gao et al., 2016; Highfield et al., 2009; Huaxu et al., 2017; Liu et al., 2017). Figure 3 shows that, although the present work adopted the simplest and less active Au-TiO_2 catalyst, a 30%–50% increase in H_2 productivity was observed compared with previously reported values. Considering the energy donor as the absorbed sunlight and the acceptor as the photo-thermal reaction,

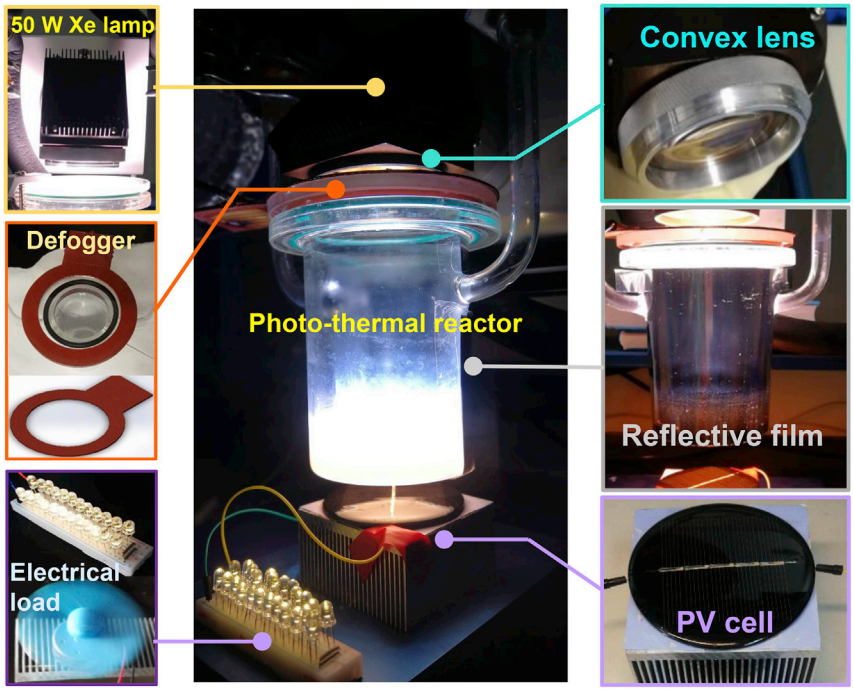

Figure 2. Selective Absorption for Photo-Thermal Hydrogen

Experimental apparatus for the cascading production of photo-thermal H_2 and electricity from full-spectrum sunlight.

the acceptor side responds better to the charge carriers from the UV-vis band and phonons from the IR band. If the catalyst absorption is monotonously expanded, the additional Vis-NIR band may provide more photons with lower energy. Such Vis-NIR charge carriers have insufficient energy for H_2 generation but may produce phonon heat to inhibit the transfer of charge carriers. Owing to spectral selectivity, photo-thermocatalysis avoided handling the Vis-NIR band, increasing the H_2 productivity.

Figure 3 suggests that solar concentration plays an important role in photo-thermal H_2 generation. Solar concentration pressurizes the photon gas before it enters the turbine (Bejan, 2016), improving the capacity of sunlight to do work. In concentrated sunlight-H_2 conversion, the capacity to do work appears as H_2 productivity. In the present work, the H_2 productivity increases linearly as the sunlight is concentrated to 3–15 suns. The primary cause for such linear promotion is the densified charge carrier flow and localized surface heating under the solar concentration. The charge carrier flow may be explained by electromagnetic simulation, where an SPR Au localized electrical field is observed. The localized electricity field can selectively absorb the UV-vis band and channel the charge carrier generation process near the TiO_2 surface (Figures S4A and S4B). This can avoid the bulk phase recombination loss, especially under the concentrated sunlight (Sigle et al., 2015). Furthermore, the effect of concentrated solar heating at 35°C–85°C and C = 5–15 (Figures S5A and S5B) increased the H_2 production rate by two to three times. The reason is that the thermal effect activated more adsorbed molecules to react with the surface charge carriers, suppressing the competent process of surface recombination (Panayotov and Morris, 2016). In comparison, the pure semiconductor photocatalytic H_2 was seldom explored at a concentration ratio higher than C = 6 (Wei et al., 2018). On the one hand, the SPR effect in the present work may avoid heating from the excessive IR band or bulk recombination, which can reduce the charge carrier mobility in purely semiconductor photocatalysis (Neumann et al., 2013). On the other hand, the IR heat-assisted surface reaction avoided the loss of IR sunlight quality to waste heat in pure semiconductor photocatalysis. Therefore, the photo-thermocatalysis in this work presents an opportunity to increase the solar concentration.

We expected an increase in the ability to generate H_2 under concentrated sunlight. A breakthrough made by Turner et al. (Khaselev and Turner, 1998). promoted the sunlight-photocurrent efficiency from 7% to 12.4% for a photo-electrochemical (PEC) cell by elevating the solar concentration to C = 11.9. The results of Turner et al. encouraged us to measure the photocurrent for Au-TiO_2 nanoparticles, which absorbs a

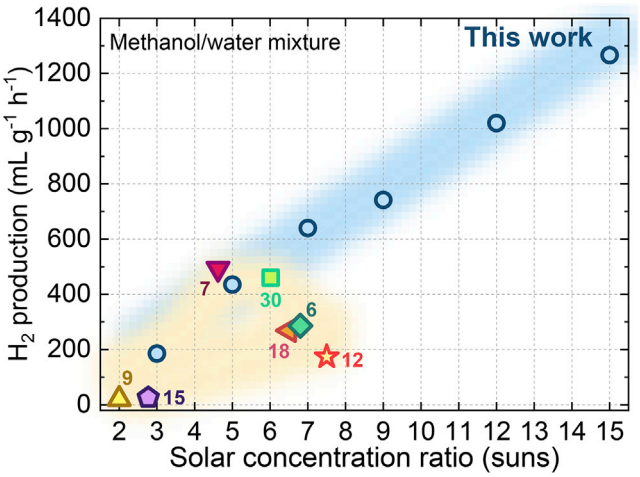

Figure 3. Photo-Thermal H_2 Generation Rate from UV-Vis/IR Spectrum in This Work and from Full-Spectrum in Previous Studies

narrow UV-vis band from the full spectrum. Figure S6 shows the continuously rising shape of the transient photocurrent character. If the transient photocurrent has a decay spike under the concentrated sunlight, there may be a possible aggregation of the energy loss in surface recombination (Sigle et al., 2015; Xue et al., 2017). The likely reason is a steady surface reaction coupled with an ever-increasing surface charge carrier productivity; thus, excessive charge carriers from the broad band may be dissipated in the recombination. Here, the selective absorption only generates charge carriers from the UV/Vis-IR narrow band (see absorptivity curve measured in Figure S3 and the absorption of Au nanoparticles simulated in Figure S4C). Moreover, no spike is observed in the transient photocurrent, indicating no charge accumulation during the test. We collected the steady photocurrent under different solar concentration values and depicted the results in Figure 4. In the present work, the steady photocurrent increases linearly from 0.20 to 1.30 μA with the concentration ratio of *C*. Individual photocatalysis typically shows a logarithmic photocurrent increase with solar concentration, slower than the linear increase (Bell et al., 2013). Using the UV/Vis-IR narrow band absorption, this work avoids the ever-increasing recombination loss in individual photocatalysis (Pihosh et al., 2015), reducing the irreversibility from the Vis-NIR band.

Figure 5A presents the influence of the catalyst mass concentration on photo-thermal H_2 generation. The effects differ in three conditions. The first is a condition of 0.1–0.5 g L^{-1} and high solar concentration (the red region), with a H_2 generation rate <30 mL h^{-1} even at $C = 15$. Although the solar concentration is high, the low catalyst concentration has weak absorption and loses the UV-vis band in transmission. The second condition is a high catalyst concentration and low solar concentration (the blue region), where the H_2 generation rate is only slightly increased to 40 mL h^{-1} at 1 g L^{-1} and $C = 7$. $C = 7$ is too weak to penetrate the nano catalyst layer and can only illuminate the catalyst nanoparticles near the skin of the reaction solution (Figure 5B). With surface reaction as the

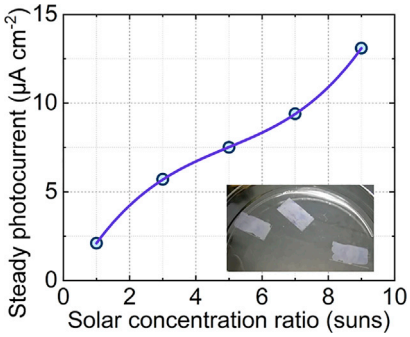

Figure 4. The Steady Photocurrent under Solar Concentration of *C* = 1–9
For experimental details see Figure S13.

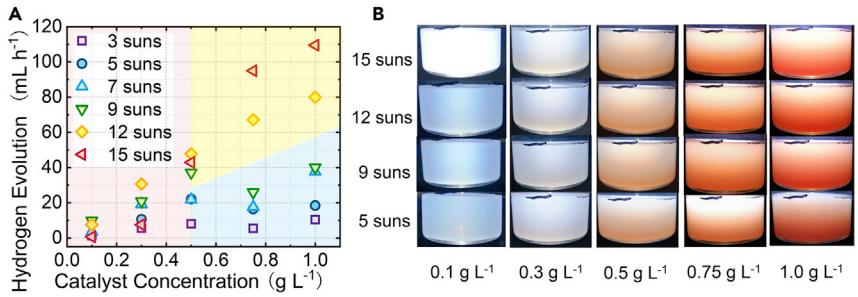

Figure 5. The Photo-Thermal Reacion under Various Solar Concentration and Catalyst Concentration

(A) Influence of catalyst mass concentration (0.1–1.0 g L^{-1}) on H_2 production rate.

(B) The appearance of the reaction solution of different volume concentrations under 5–15 suns.

rate-determining step, most surface charge carriers recombine, limiting the H_2 production on each catalyst particle. As the solution skin only contains a part of all suspended catalysts, the H_2 production rate of the solution is limited as a result. The third condition (the yellow region) reveals a strong interaction between the high solar concentration and high catalyst concentration. Compared with $C < 10$, the UV-vis sunlight at $C = 15$ may be intensive enough to easily arrive at each nanocatalyst particle of 1.0 g L^{-1} (Figure 5B), elevating the rate of H_2 conversion to the highest level of 110 mL h^{-1}.

We compared the photo-thermocatalysis method with the state-of-the-art solar thermocatalysis method where the concentrated full-spectrum sunlight as a heat source drives the water-splitting reaction for H_2 (Hong et al., 2005). Such kind of solar thermochemical water splitting thermodynamically requires a reaction temperature over 2,500°C (Fletcher and Moen, 1977). A recent benchmark is the 100 kWth pilot by Steinfeld et al. (Villasmil et al., 2017). By multistep processes instead of direct process (Steinfeld, 2002; Gokon et al., 2013), the solar-to-hydrogen efficiency was elevated to 3% with high-grade input of 1,827°C heat at >3,000 suns. Jin et al. proposed solar-driven methanol decomposition for hydrogen at temperature of 200°C and solar-to-hydrogen efficiency achieved by 45% (Hong et al., 2005, 2012). In Figure 6, pure thermocatalysis provides a 300–1,400 mL g_{cat}^{-1} h^{-1} H_2 generation rate (Caravaca et al., 2016; Caudillo-Flores et al., 2019; Fang et al., 2019; Kuo et al., 2019; Papavasillou et al., 2004; Pu et al., 2019; Sun et al., 2019), requiring a reaction temperature of 200°C–300°C (for a parabolic solar concentrator Hong et al., 2012, see Table S2). With the same reactant and a similar H_2 generation rate, the present work reduces the solar concentration to $C = 15$. The main reason is that solar thermocatalysis begins with the conversion of full-spectrum sunlight into reaction heat. Reaction heat is transferred as a phonon or the thermal motion of molecules, both of which have a disordered state of movement. To drive the ordered exchange of electrons in a reaction, the disordered phonon or the thermal motion requires high temperatures to overcome the high activation energy barrier. Furthermore, the high-concentration sunlight energy is like that of a compressed photon gas with high work availability, suffering energy degradation and arising the irreversibility in the solar thermocatalysis process. Therefore, it is important to consider lowering the solar concentration ratio. By contrast, there is a possibility for the proposed photo-thermal catalysis process to reduce the irreversibility. This is because the photochemical component provides a direct photon-H_2 conversion with lower activation energy barrier, rather than only relying on the thermal activation of molecules (Wang et al., 2018a). In addition, the thermal component enables more activated reactant molecules to pass the activation energy barrier and promotes the H_2 generation rate. In this case, a low solar concentration would be enough for the need of the photo-thermal catalysis process.

Transmitted Sunlight for Photovoltaics

The measured transmitted sunlight is distributed in the 600- to 1,200-nm Vis-NIR narrow band, accounting for 5%–20% of the full-spectrum energy (Figures S3, S7A, and S7B). Therefore, we integrated the commercial 2.5-V P-type mono-crystalline silicon PV cell with the 1.2- to 1.3-eV bandgap, which is expected to accommodate the transmitted energy. Then, we assessed the power generation capability by a voltammetry measuring method (Kiermasch et al., 2019), which ran a voltage sweep on a high-sensitivity programmable electrical load (details in Figure S14). For each case, the voltage-current curve of the PV cell was monitored to find the maximum power output (see Figures S8A–S8F). As a comparison experiment, the individual PV was also studied using full-spectrum input. Figure 7A shows the electricity output of the integrated PV. Using the 600- to 1,200-nm narrow band energy, the PV produces 0.3–0.6 W electricity. Since

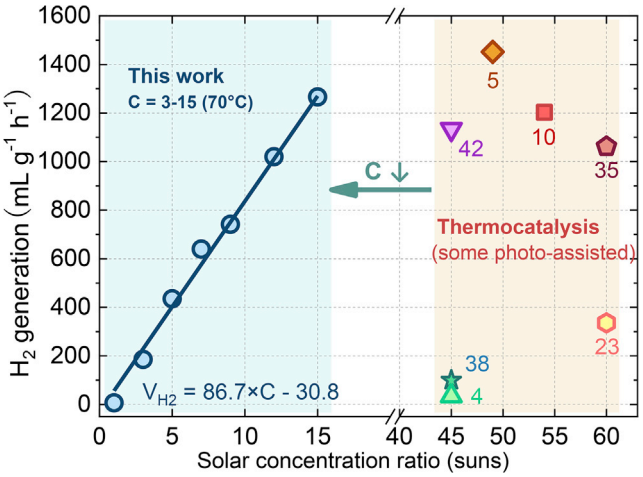

Figure 6. Solar Concentration Ratio Required by Photo-Thermally Driven or Thermally Driven Reaction

the PV electricity increases with the transmitted Vis-NIR band, the PV maximum power output increases linearly with the solar concentration ranging from 1 to 15 and decreases with the catalyst concentration varying from 0.1 to 1.0 g L^{-1}. The PV output at any condition can drive the continuous operation of a motor fan or 25 LEDs (Videos S2 and S3).

Figure 7B depicts the efficiency of the same PV cell with or without the integration with photo-thermal reactions. For the same solar concentration *C*, the PV efficiency continuously increases from <10% (individual PV) to 40% (1.0 g L^{-1}) when integrated with the photo-thermal reaction at higher catalyst concentrations because of the decreasing PV heat relaxation loss in the UV/IR band, which is intercepted by the photo-thermal reaction solution for H_2 generation. For the same catalyst concentration, the PV efficiency behaves differently with the increasing solar concentration. For the individual PV or integrated PV with <0.5 g L^{-1}, the PV efficiency continuously decreases from 35% to <10% with increasing *C*. The reason is the aggregated heat recombination caused by an increasing sunlight intensity in UV and IR bands transmitted from the reaction solution. The highest PV efficiency of ~40% was found when the PV cell was integrated with the catalyst concentration of 0.5–1.0 g L^{-1}. Under this condition, the UV/IR band from the 15-sun concentrated sunlight is fully intercepted by the photo-thermal reaction. A sufficient amount and the exact band of Vis-NIR sunlight is transmitted, coinciding with the photovoltaic bandgap and improving the PV efficiency.

Efficiency of the Co-generation System

In this section, we assessed the performance of the synergic system of both H_2 and electricity. Equation 1 was used to describe the overall efficiency of sunlight conversion into H_2 and electricity.

$$\eta_{sys} = \frac{\Delta G_{H_2} \cdot (V_{H_2}/22.4) + U_{PV} \cdot I_{PV}}{C \cdot \int_{300nm}^{2500nm} I(\lambda) d\lambda + \Delta G_{CH_3OH} \cdot n_{CH_3OH}} \quad \text{(Equation 1)}$$

In Equation 1, the denominator consists of two terms. One is the production of the Gibbs free energy in H_2 (ΔG_{H2}) multiplied by the molar amount of H_2 ($V_{H2}/22.4$), representing the chemical energy output from the UV-vis/IR band. Another is the PV power U_{PV} I_{PV}, representing the electricity output from the Vis-NIR band. The nominator is the full-spectrum spectral energy $\int_{300nm}^{2500nm} I(\lambda) d\lambda$ multiplied by the solar concentration ratio *C*, representing the input full-spectrum concentrated sunlight. The input Gibbs free energy of methanol consumed by the photo-thermal reaction is also considered as $\Delta G_{CH3OH} \cdot n_{CH3OH}$, calculated according to the consumption ratio provided in the isotope tracer experiment (Fang et al., 2019). The reason for using ΔG_{H_2} is to equalize the energy grade of the chemical energy in H_2 to that of the electricity (Coridan et al., 2015).

Using Equation 1, we can calculate the overall efficiency according to *C*, n_{H_2}, and P_{PV} from the experimental results (the calculation process is presented in Supplemental Information). As depicted in Figure 8, the overall system efficiency increases with the solar concentration ratio *C*, finally reaching 3.8%–4.2% at *C* = 12–15. The comparisons were also performed for the experimental results from the individual cases of

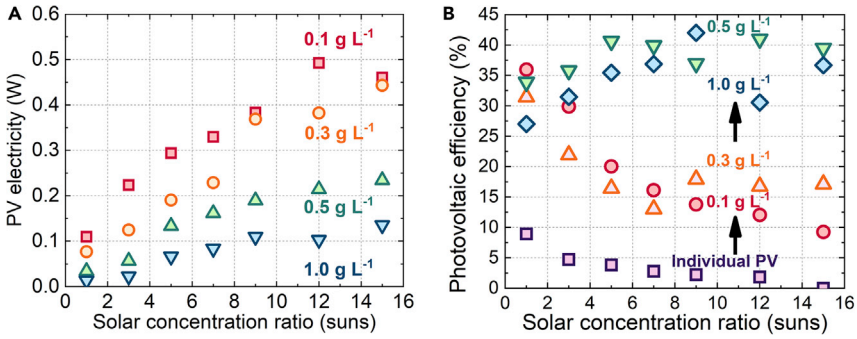

Figure 7. Transmitted Sunlight for Photovoltaics

Measured PV (A) electricity output and (B) efficiency with or without integration with the photo-thermal reaction.

PV and photo-thermal H_2 generation (the experimental setup is presented in Supplemental Information). With the increase in *C*, the individual PV efficiency continuously decreases to 0.2% and the individual photo-thermal H_2 efficiency slightly increases to 2%. In comparison, the hybrid system efficiency is 3 percentage points higher than both individual cases at a high solar concentration ($C > 7$).

To further reveal the energy loss reduction mechanism at each spectral band, we performed an energy flow analysis for the hybrid system (the calculation process is presented in Supplemental Information). The results are shown as the Sankey diagram in Figure 9 (data listed in Table S3). For comparison, the individual cases were also assessed (Figures S9A and S9B and Table S3). From the flow direction of the solar energy, the system can be assessed in the upstream (solar concentration and spectral selection) and downstream processes (photo-thermocatalysis and PV generation).

In upstream processes, the input full-spectrum sunlight is first concentrated to intensify the photon flux and improve the capacity to do work, accounting for 9.75% of the system input for optical loss. Then, in the spectral selection process, the concentrated sunlight is selected into UV-vis/IR and Vis-NIR bands. Since part of the Vis-NIR band can be easily scattered in spectral selection, we used the reflection film to partly recover the scattered sunlight (accounting for 4.88% in system input) for PV conversion. In comparison, the individual photo-thermocatalysis (Figure S9A) did not utilize but dissipated the Vis-NIR band as transmission and scattering losses, comprising 38.63% of the system input.

After the spectral selection, the downstream processes included the photovoltaic and photo-thermocatalytic processes. For the photovoltaic process, the case of the integrated PV cell received the Vis-NIR band (22.78% in system input). The photon energy of 1.1–1.3 eV at the Vis-NIR band coincided with the bandgap of the P-type monocrystalline silicon and had low recombination loss in the PV cell. Thus, the PV generated electricity was 2.57% in the system input, with 20.21% of waste heat. In the case of individual PV (Figure S9B), the mono-silicon PV cell received the full-spectrum concentrated sunlight (90.25%). A considerable amount of the UV-vis band (2–4 eV) and IR band (<1.1 eV) was dissipated through heat relaxation when received by the mono-Si bandgap of 1.1–1.3 eV. In addition, the UV and IR heat relaxation reduced the charge mobility and further aggregated the recombination loss in the Vis-NIR band. Therefore, the individual PV produced 88.75% waste heat and only 1.90% electricity output.

For photo-thermocatalysis, the UV-vis band (24.67%) and IR band (22.95%) were absorbed to generate charge carriers and phonons. Phonons from the IR band joined the UV-vis charge carriers for H_2 production and collaborated for the 1.71% photo-thermal H_2 production. In the first step, the concentrated UV-vis band generated charge carriers gathered on the catalyst surface. Then, the IR-induced localized heating activated more adsorbed molecules to react with the surface charge carriers to generate H_2, suppressing the competing process of surface recombination (Panayotov and Morris, 2016). In individual photocatalysis, the IR band is expected to generate charge carriers through up-conversion, which combines two NIR or IR photons into one UV or Vis photon. Although the up-conversion is innovative and worth studying, the highest ratio ever achieved for up-conversion is 0.1%–4.0%; thus, it is not ready for potential industrial applications (Zhang et al., 2017). In contrast, photo-thermocatalysis uses IR heat as the assistive diving force and directly elevates the energy of the IR band to chemical energy stored in the H-H bond. Such elevation in the IR energy grade competes with the heat relaxation process, reducing the loss of the IR band to waste heat.

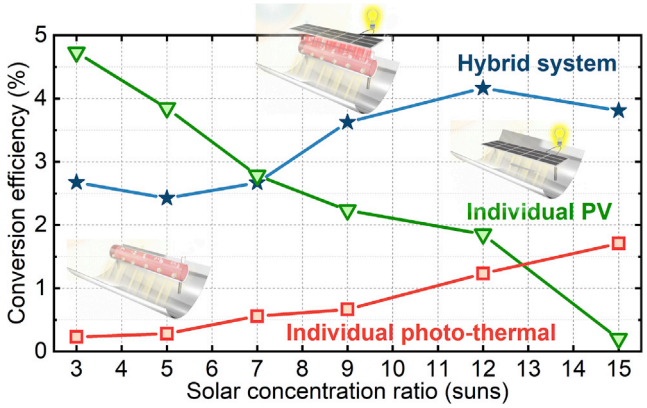

Figure 8. Efficiency of the Co-generation System

Overall efficiency of the hybrid system in comparison with the individual PV and individual photo-thermocatalysis.

The results of the hybrid system reveal the potential of the full-spectrum cascade conversion for photothermal H_2 and PV. One advantage of the hybrid system is its cost-effectiveness in scalable applications. Reducing the dependency on specific and sophisticated materials, this system adopts commercial P25 TiO_2 loaded with 5 mol% Au and the commercial mono-silicon PV cell. Such simplicity in materials can help save the synthesis steps for an economical scale-up (Tang et al., 2019). The input solar concentration ratio of 15 suns in the experiments can be found on a parabolic or Fresnel solar collector. Such solar collectors at 40–50 suns have been commonly used for 30–40 years in solar thermal power applications, and the results of this work are encouraging in saving the area of the collector mirror. Although such solar concentrators have 60%–70% optical efficiency, this value may exceed 80% with double-axis tracking (Wang et al., 2018b). The hybrid system can also accommodate the innovations in materials technology, such as structure engineered catalyst (narrow-bandgap semiconductor or non-precious SPR metal loading) and third-generation PV cells (GaAs) (NREL, 2019), with an expected 5–10 percentage points of increase in the overall efficiency.

The sunlight intensity intrinsically varies throughout the year. In general, the production of solar fuel and solar electricity should consider the average annual utilization, which is an important indicator of the system availability to solar energy. For the proposed hybrid system, a satisfying annual utilization is expected because the system integrates the PV power output and H_2 energy storage. In summer days, the system uses abundant solar irradiation to generate more H_2 for long-term storage. When solar irradiation decreases in winter, the stored H_2 can generate electricity in a fuel cell or a gas turbine, compensating the gap between the PV output and the electricity demand. Therefore, the proposed hybrid system provides a potential pathway for highly cost-effective sunlight utilization throughout the year.

In summary, the present work demonstrated a concentrated solar energy system co-producing H_2 and electricity from a cascade pathway of solar spectrum. In the experimental design, a simple Au-TiO_2 water-splitting reaction was accommodated as a spectral selector, which absorbed the UV-vis/IR band for photo-thermal H_2 and transmitted the Vis-NIR band. By selecting the high-grade UV-vis band for charge carriers and collaborating with the IR heat, the H_2 generation rate increased super-linearly at 3–15 suns to the highest rate of 1,260 mL g h^{-1}. The transmitted Vis-NIR band coincided with the PV bandgap, reducing the heat relaxation and recombination thus retaining high efficiency under concentrated sunlight. An overall efficiency of 4.2% was obtained at 12 suns. The energy flow analysis demonstrated a reduced energy loss in full spectrum compared with the individual photo-thermocatalysis or the PV cell. Reduction in solar concentration and the simplicity of materials enables the control of the construction cost of industrial solar collectors. Furthermore, the adjustable H_2/electricity output can resolve the fundamental concern on the intrinsic and seasonal nature of sunlight. Therefore, the hybrid system can be the basis for concurrent H_2 and electricity harnessing by cascading the full-spectrum concentrated sunlight with integrated conversion processes and can be an alternative for individual PV, PEC, or photocatalysis systems in the future.

Limitations of the Study

An optimized design of nanostructure (like core-shell or 2D) and material (like TiO_x) could potentially improve the spectral selectivity and reaction activity of the current catalyst. A simulation on the reactor

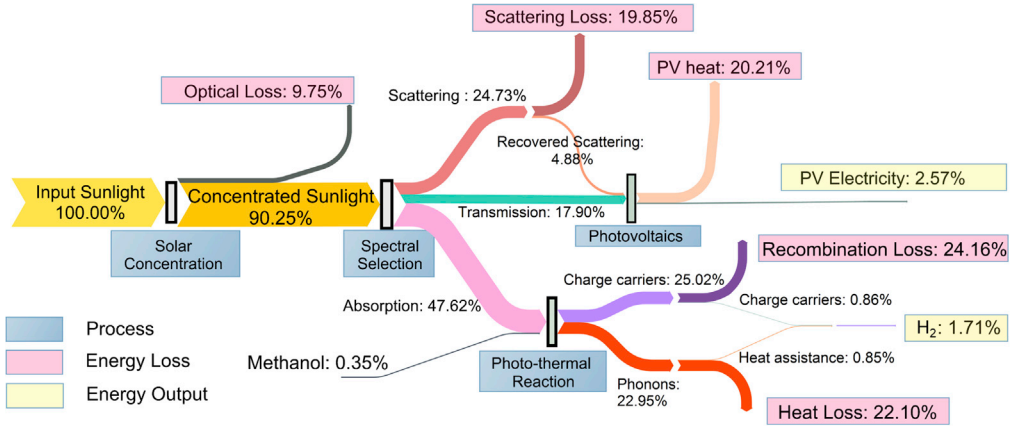

Figure 9. Energy Flow Analysis of the Hybrid System

scale can help further understand the influence of solar concentration ratio and mass concentration on system overall efficiency, facilitating the potential application of the proposed system.

METHODS

All methods can be found in the accompanying Transparent Methods supplemental file.

SUPPLEMENTAL INFORMATION

Supplemental Information can be found online at https://doi.org/10.1016/j.isci.2020.101012.

ACKNOWLEDGMENTS

This work is supported by the Basic Science Center Program for Ordered Energy Conversion of the National Natural Science Foundation of China (No. 51888103), the National Natural Science Foundation of China (No. 51590904), and the Key Research Program of the Chinese Academy of Sciences (No. KFZD-SW-418).

AUTHOR CONTRIBUTIONS

Conceptualization, S.T. and H.H.; Methodology, S.T. and J.S.; Investigation, S.T., X.X., and W.Y.; Resources, S.T., X.X., and W.Y.; Writing – Original Draft, S.T. and H.H.; Writing – Review & Editing, H.H., S.T., L.W., and Y.X.; Visualization – S.T.; Funding Acquisition, H.H. and H.J.; Supervision, H.H., H.J., and Y.X.

DECLARATION OF INTERESTS

The authors declare no competing interests.

Received: February 3, 2020
Revised: February 13, 2020
Accepted: March 19, 2020
Published: April 24, 2020

REFERENCES

Bejan, A. (2016). Advanced Engineering Thermodynamics (John Wiley & Sons, Inc.).

Bell, S., Will, G., and Bell, J. (2013). Light intensity effects on photocatalytic water splitting with a titania catalyst. Int. J. Hydr. Energy *38*, 6938–6947.

Cao, Y., Zhou, P., Tu, Y., Liu, Z., Dong, B.-W., Azad, A., Ma, D., Wang, D., Zhang, X., Yang, Y., et al. (2019). Modification of TiO2 nanoparticles with organodiboron molecules inducing stable surface Ti3+ complex. iScience *20*, 195–204.

Caravaca, A., Daly, H., Smith, M., Mills, A., Chansai, S., and Hardacre, C. (2016). Continuous flow gas phase photoreforming of methanol at elevated reaction temperatures sensitised by Pt/TiO2. React. Chem. Eng. *1*, 649–657.

Caudillo-Flores, U., Agostini, G., Marini, C., Kubacka, A., and Fernandez-Garcia, M. (2019). Hydrogen thermo-photo production using Ru/TiO2: heat and light synergistic effects. Appl. Catal. B Environ. *256*, 117790.

Chiarello, G.L., Aguirre, M.H., and Selli, E. (2010). Hydrogen production by photocatalytic steam reforming of methanol on noble metal-modified TiO2. J. Catal. *273*, 182–190.

Chiarello, G.L., Dozzi, M.V., Scavini, M., Grunwaldt, J.D., and Selli, E. (2014). One step

flame-made fluorinated Pt/TiO2 photocatalysts for hydrogen production. Appl. Catal. B Environ. *160*, 144–151.

Coridan, R.H., Nielander, A.C., Francis, S.A., Mcdowell, M.T., Dix, V., Chatman, S.M., and Lewis, N.S. (2015). Methods for comparing the performance of energy-conversion systems for use in solar fuels and solar electricity generation. Energy Environ. Sci. *8*, 2886–2901.

Elbanna, O., Kim, S., Fujitsuka, M., and Majima, T. (2017). TiO2 mesocrystals composited with gold nanorods for highly efficient visible-NIR-photocatalytic hydrogen production. Nano Energy *35*, 1–8.

Fang, S., Sun, Z., and Hu, Y.H. (2019). Insights into the thermo-photo catalytic production of hydrogen from water on a low-cost NiOx-loaded TiO2 catalyst. ACS Catal. *9*, 5047–5056.

Fletcher, E.A., and Moen, R.L. (1977). Hydrogen and oxygen from water. Science *197*, 1050–1056.

Gao, M., Connor, P.K.N., and Ho, G.W. (2016). Plasmonic photothermic directed broadband sunlight harnessing for seawater catalysis and desalination. Energy Environ. Sci. *9*, 3151–3160.

Ghoussoub, M., Xia, M., Duchesne, P.N., Segal, D., and Ozin, G. (2019). Principles of photothermal gas-phase heterogeneous CO2 catalysis. Energy Environ. Sci. *12*, 1122–1142.

Gokon, N., Sagawa, S., and Kodama, T. (2013). Comparative study of activity of cerium oxide at thermal reduction temperatures of 1300–1550°C for solar thermochemical two-step water-splitting cycle. Int. J. Hydr. Energy *38*, 14402–14414.

Highfield, J.G., Chen, M.H., Nguyen, P.T., and Chen, Z. (2009). Mechanistic investigations of photo-driven processes over TiO2 by in-situ DRIFTS-MS: Part 1. Platinization and methanol reforming. Energy Environ. Sci. *2*, 991–1002.

Hong, H., Jin, H., Ji, J., Wang, Z., and Cai, R. (2005). Solar thermal power cycle with integration of methanol decomposition and middle-temperature solar thermal energy. Sol. Energy *78*, 49–58.

Hong, H., Liu, Q., and Jin, H. (2012). Operational performance of the development of a 15 kW parabolic trough mid-temperature solar receiver/reactor for hydrogen production. Appl. Energy *90*, 137–141.

Huaxu, L., Fuqiang, W., Ziming, C., Shengpeng, H., Bing, X., Xiangtao, G., Bo, L., Jianyu, T., Xiangzheng, L., Ruiyang, C., et al. (2017). Analyzing the effects of reaction temperature on photo-thermo chemical synergetic catalytic water splitting under full-spectrum solar irradiation: an experimental and thermodynamic investigation. Int. J. Hydr. Energy *42*, 12133–12142.

IEA (2019). The Future of Hydrogen. www.iea.org/publications/reports/thefutureofhydrogen/.

Jia, J., O'brien, P.G., He, L., Qiao, Q., Fei, T., Reyes, L.M., Burrow, T.E., Dong, Y.C., Liao, K., Varela, M., et al. (2016). Visible and near-infrared photothermal catalyzed hydrogenation of gaseous CO2 over nanostructured Pd@Nb2O5. Adv. Sci. *3*, 13.

Khaselev, O., and Turner, J.A. (1998). A monolithic photovoltaic-photoelectrochemical device for hydrogen production via water splitting. Science *280*, 425–427.

Kiermasch, D., Gil-Escrig, L., Bolink, H.J., and Tvingstedt, K. (2019). Effects of masking on open-circuit voltage and fill factor in solar cells. Joule *3*, 16–26.

Li, X., Ni, G., Cooper, T., Xu, N., Li, J., Zhou, L., Hu, X., Zhu, B., Yao, P., and Zhu, J. (2019a). Measuring conversion efficiency of solar vapor generation. Joule *3*, 1798–1803.

Li, Y., Wang, C., Song, M., Li, D., Zhang, X., and Liu, Y. (2019b). TiO2-x/CoOx photocatalyst sparkles in photothermocatalytic reduction of CO2 with H2O steam. Appl. Catal. B Environ. *243*, 760–770.

Kuo, M.-T., Chen, Y.-Y., Hung, W.-Y., Lin, S.-F., Lin, H.-P., Hsu, C.-H., Shih, H.-Y., Xie, W.-A., and Li, S.-N. (2019). Synthesis of mesoporous CuFe/silicates catalyst for methanol steam reforming. Int. J. Hydr. Energy. *44*, 14416–14423.

Li, Y.F., Lu, W., Chen, K., Duchesne, P., Jelle, A., Xia, M.K., Wood, T.E., Ulmer, U., and Ozin, G.A. (2019c). Cu atoms on nanowire Pd/HyWO3-x, bronzes enhance the solar reverse water gas shift reaction. J. Am. Chem. Soc. *141*, 14991–14996.

Liang, L., Li, X., Sun, Y., Tan, Y., Jiao, X., Ju, H., Qi, Z., Zhu, J., and Xie, Y. (2018). Infrared light-driven CO2 overall splitting at room temperature. Joule *2*, 1004–1016.

Liu, G., Ma, L., Yin, L.-C., Wan, G., Zhu, H., Zhen, C., Yang, Y., Liang, Y., Tan, J., and Cheng, H.-M. (2018). Selective chemical epitaxial growth of TiO2 Islands on ferroelectric PbTiO3 crystals to boost photocatalytic activity. Joule *2*, 1095–1107.

Liu, X., Iocozzia, J., Wang, Y., Cui, X., Chen, Y., Zhao, S., Li, Z., and Lin, Z. (2017a). Noble metal-metal oxide nanohybrids with tailored nanostructures for efficient solar energy conversion, photocatalysis and environmental remediation. Energy Environ. Sci. *10*, 402–434.

Liu, X., Ye, L., Ma, Z., Han, C., Wang, L., Jia, Z., Su, F., and Xie, H. (2017b). Photothermal effect of infrared light to enhance solar catalytic hydrogen generation. Catal. Commun. *102*, 13–16.

Neumann, O., Urban, A.S., Day, J., Lal, S., Nordlander, P., and Halas, N.J. (2013). Solar vapor generation enabled by nanoparticles. ACS Nano *7*, 42–49.

NREL (2019). Best Research-Cell Efficiency Chart. http://www.nrel.gov/pv/assets/images/efficiency-chart.png.

Ozin, G.A. (2017). "One-Pot" solar fuels. Joule *1*, 19–23.

Panayotov, D.A., and Morris, J.R. (2016). Surface chemistry of Au/TiO2: Thermally and photolytically activated reactions. Surf. Sci. Rep. *71*, 77–271.

Papavasillou, J., Avgouropoulos, G., and Ioannides, T. (2004). Production of hydrogen via combined steam reforming of methanol over CuO-CeO2 catalysts. Catal. Commun. *5*, 231–235.

Pihosh, Y., Turkevych, I., Mawatari, K., Uemura, J., Kazoe, Y., Kosar, S., Makita, K., Sugaya, T., Matsui, T., Fujita, D., et al. (2015). Photocatalytic generation of hydrogen by core-shell WO(3)/BiVO(4) nanorods with ultimate water splitting efficiency. Sci. Rep. *5*, 11141.

Pinaud, B.A., Benck, J.D., Seitz, L.C., Forman, A.J., Chen, Z., Deutsch, T.G., James, B.D., Baum, K.N., Baum, G.N., Ardo, S., et al. (2013). Technical and economic feasibility of centralized facilities for solar hydrogen production via photocatalysis and photoelectrochemistry. Energy Environ. Sci. *6*, 1983–2002.

Pu, Y.-C., Li, S.-R., Yan, S., Huang, X., Wang, D., Ye, Y.-Y., and Liu, Y.-Q. (2019). An improved Cu/ZnO catalyst promoted by Sc2O3 for hydrogen production from methanol reforming. Fuel *241*, 607–615.

Qi, Y., Zhao, Y., Gao, Y., Li, D., Li, Z., Zhang, F., and Li, C. (2018). Redox-Based visible-light-driven Z-scheme overall water splitting with apparent quantum efficiency exceeding 10%. Joule *2*, 2393–2402.

Sigle, D.O., Zhang, L., Ithurria, S., Dubertret, B., and Baumberg, J.J. (2015). Ultrathin CdSe in plasmonic nanogaps for enhanced photocatalytic water splitting. J. Phys. Chem. Lett. *6*, 1099–1103.

Steinfeld, A. (2002). Solar hydrogen production via a two-step water-splitting thermochemical cycle based on Zn/ZnO redox reactions. Int. J. Hydr. Energy *27*, 611–619.

Sun, Z.X., Fang, S.Y., Lin, Y., and Hu, Y.H. (2019). Photo-assisted methanol steam reforming on solid solution of Cu-Zn-Ti oxide. Chem. Eng. J. *375*, 121909.

Tang, S., Hong, H., Jin, H., and Xuan, Y. (2019). A cascading solar hybrid system for co-producing electricity and solar syngas with nanofluid spectrum selector. Appl. Energy *248*, 231–240.

Tang, S., Hong, H., Sun, J., and Qu, W. (2018). Efficient path of distributed solar energy system synergetically combining photovoltaics with solar-syngas fuel cell. Energ. Convers. Manage. *173*, 704–714.

Tang, S.L., Sun, J., Hong, H., and Liu, Q.B. (2017). Solar fuel from photo-thermal catalytic reactions with spectrum-selectivity: a review. Front. Energy *11*, 437–451.

Tavasoli, A., and Ozin, G. (2018). Green syngas by solar dry reforming. Joule *2*, 571–575.

Villasmil, W., Cooper, T., Koepf, E., Meier, A., and Steinfeld, A. (2017). Coupled concentrating optics, heat transfer, and thermochemical modeling of a 100-kW th high-temperature solar reactor for the thermal dissociation of ZnO. J. Sol. Energy Eng. *139*, 021015.

Wang, Q., Hisatomi, T., Jia, Q., Tokudome, H., Zhong, M., Wang, C., Pan, Z., Takata, T., Nakabayashi, M., and Shibata, N. (2016). Scalable water splitting on particulate photocatalyst sheets with a solar-to-hydrogen energy conversion efficiency exceeding 1%. Nat. Mater. *15*, 611–615.

Wang, L., Ghoussoub, M., Wang, H., Shao, Y., Sun, W., Tountas, A.A., Wood, T.E., Li, H., Loh, J.Y.Y., Dong, Y., et al. (2018a). Photocatalytic hydrogenation of carbon dioxide with high selectivity to methanol at atmospheric pressure. Joule *2*, 1369–1381.

Wang, R., Qu, W., Hong, H., Sun, J., and Jin, H. (2018b). Experimental performance of 300 kWth prototype of parabolic trough collector with rotatable axis and irreversibility analysis. Energy *161*, 595–609.

Wei, Q.Y., Yang, Y., Liu, H.J., Hou, J.Y., Liu, M.C., Cao, F., and Zhao, L. (2018). Experimental study on direct solar photocatalytic water splitting for hydrogen production using surface uniform concentrators. Int. J. Hydr. Energy *43*, 13745–13753.

Weinstein, L.A., Mcenaney, K., Strobach, E., Yang, S., Bhatia, B., Zhao, L., Huang, Y., Loomis, J., Cao, F., Boriskina, S.V., et al. (2018). A hybrid electric and thermal solar receiver. Joule *2*, 962–975.

Xu, N., Zhu, P., Sheng, Y., Zhou, L., Li, X., Tan, H., Zhu, S., and Zhu, J. (2020). Synergistic tandem solar electricity-water generators. Joule *4*, 347–358.

Xue, C., An, H., Yan, X., Li, J., Yang, B., Wei, J., and Yang, G. (2017). Spatial charge separation and transfer in ultrathin CdIn2S4/rGO nanosheet arrays decorated by ZnS quantum dots for efficient visible-light-driven hydrogen evolution. Nano Energy *39*, 513–523.

Yang, Z., Jiang, Y., Zhang, W., Ding, Y., Jiang, Y., Yin, J., Zhang, P., and Luo, H. (2019). Solid-state, low-cost, and green synthesis and robust photochemical hydrogen evolution performance of ternary TiO2/MgTiO3/C photocatalysts. iScience *14*, 15–26.

Zhang, W., Yang, S., Li, J., Gao, W., Deng, Y., Dong, W., Zhao, C., and Lu, G. (2017). Visible-to-ultraviolet Upconvertion: energy transfer, material matrix, and synthesis strategies. Appl. Catal. B Environ. *206*, 89–103.

Zhao, X., Luo, W., Feng, J., Li, M., Li, Z., Yu, T., and Zou, Z. (2014). Quantitative analysis and visualized evidence for high charge separation efficiency in a solid-liquid bulk heterojunction. Adv. Energy Mater. *4*, 1301785.

iScience, Volume *23*

Supplemental Information

Synergizing Photo-Thermal H_2 and Photovoltaics into a Concentrated Sunlight Use

Sanli Tang, Xueli Xing, Wei Yu, Jie Sun, Yimin Xuan, Lu Wang, Yangfan Xu, Hui Hong, and Hongguang Jin

Supplemental Information

Supplemental Data Items

Morphology stability and selective absorption of Au-TiO_2

To test the distribution of Au on TiO_2 nanoparticles, we examined the morphology of the nanocatalyst using scanning electron microscopy (SEM) and transmission electron microscopy (TEM). **Figure S1** shows that the catalyst is composed of TiO_2 nanoparticles of ~ 50 nm, while the Au NPs are uniformly deposited on the surface of the TiO_2 nanoparticles. High-resolution TEM in **Figure S1** shows that the average diameter of Au NPs is 10-15 nm.

The stability of the nanostructures under high-intensity sunlight was also examined. **Figures S1** and **S2** compare the TEM and SEM images before and after 40 h experiments under the sunlight intensity of 15 kW m^{-2}. The morphology of Au-TiO_2 remained stable. Neither the deposition nor the morphology of the Au nanocrystals changed after the experiments. The HRTEM image also demonstrates that the Au NPs remain an average diameter of 10–15 nm and show no sign of agglomeration after the experiment.

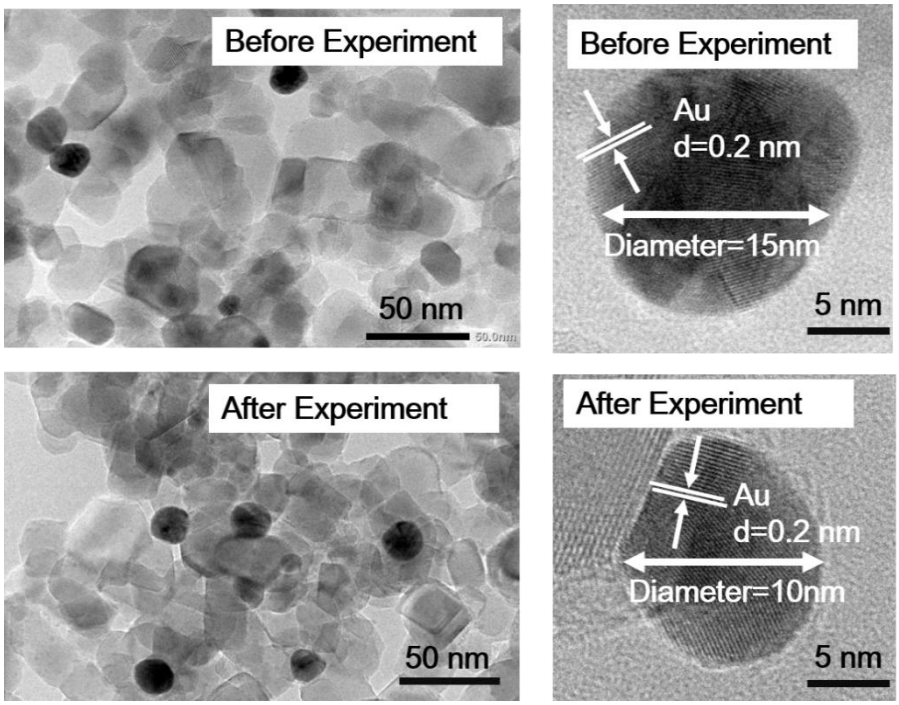

Figure S1. TEM and HRTEM image of the Au-TiO_2 photo-thermal catalyst, related to **Figure 2**.

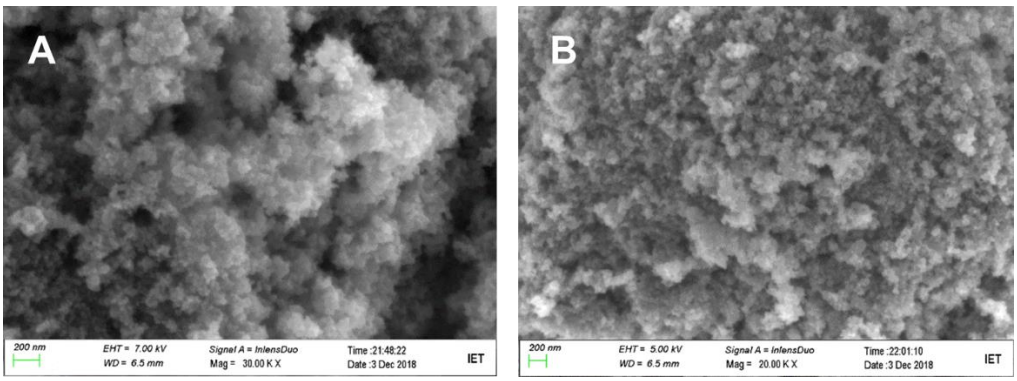

Figure S2. SEM image (A) before and (B) after 40 hours of hydrogen evolution experiments, related to **Figure 2**.

Before integrating PV into the system, we measured the transmitted sunlight intensity and spectrum distribution. The measurements were done on an Agilent Cary5000 UV-Vis-IR spectrometer. **Figure S3** shows that the unabsorbed sunlight is at the 600–1200 nm band and is close to that of a band-pass optical beam splitter (Vincenzi et al., 2010), which matches the mono-Si PV bandgap. To further adapt to various PV materials, we can conveniently shift the transmitted spectrum by controlling the size and shape of Au-TiO_2 and changing the optical thickness and mass concentration of the reaction solution. In this study, the mass concentration of 0.1–1.0 g L^{-1} can control the transmittivity at 600–1200 nm at 10–70%.

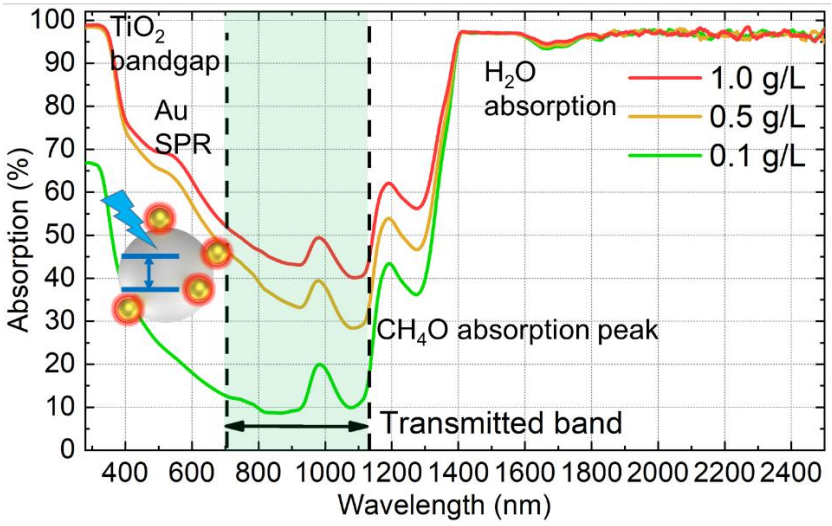

Figure S3. Absorption spectra of the reaction solution at catalyst concentration of 0.1–1.0 g L^{-1} in 10 vol. % methanol aqueous solution, related to **Figure 2** and **7**.

Simulated electromagnetic absorption of Au-TiO_2

The increase in the H_2 production rate benefits from the Au loading, which broadens the transport channel for charge carriers. We used the FEM method to simulate the effect of plasmonic Au (diameter 15 nm) on the light absorption of TiO_2 (diameter 30 nm) nanoparticles (**Figure S4A**). **Figure S4A** shows that at 400 nm wavelength, TiO_2 nanoparticles have a bulk phase absorption of ~10^2 times higher than the surface owing to the semiconductor excitation and corresponding absorption. For the wavelength at 400–600 nm, the absorption is pronounced on the surface, ~2×10^3 times the bulk of Au NPs because of the surface plasmon enhancement. Such enhancement also activates the TiO_2 surface, which has a 10^3 enhancement in the electrical field than the bulk part of TiO_2 in **Figure S4B**. **Figures S4A** and **S4B** reveal that the SPR effect of Au NPs can result in an intensified localized electric field, enhancing the charge carrier generation and separation on the surface. **Figure S4C** shows that the Au NPs at diameters of 10 and 15 nm have a stronger surface plasmon resonance (SPR) effect in the ultraviolet-visible narrow band than Pt NPs, enhancing the selectivity for transmitted sunlight.

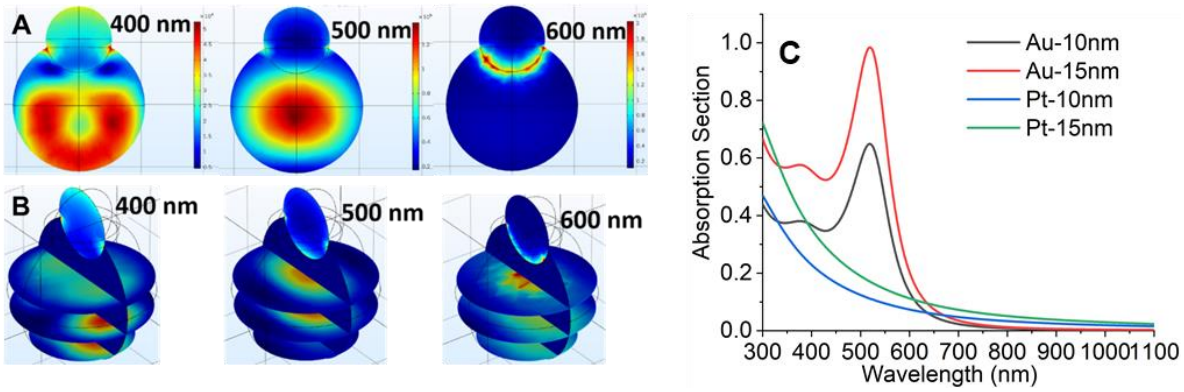

Figure S4. Electromagnetic simulation of Au-TiO_2 immersed in 10 vol % methanol aqueous solution, related to **Figure 3**. (A) The norm of the total electrical field vector and (B) the absorption of incident light under 400–600 nm irradiation. (C) The comparison of loaded metallic particles in absorption spectra.

Details for comparison with benchmark photo-thermal or thermal catalysis

Table S1 shows the details of the benchmark research in photo-thermal catalytic H_2 generation from methanol aqueous solution (see **Figure 3**). Note that some research used a strong light intensity in UV band. For convenience in comparison, the equivalent solar concentration ratio of such research was calculated by dividing the employed UV light intensity by its proportion in full-spectrum energy. In other words, the equivalent solar concentration ratio means how many suns are needed to provide the input UV light used in the reported experiment.

Table S1. Experimental details of the references, related to **Figure 3.**

Material	Intensity (kW m^{-2}) @Wavelength band	Equivalent intensity (suns)	Reaction temperature(°C)	H_2 generation rate (mL g_{cat}^{-1} h^{-1})	Reference in **Figure 3**
SiO_2/Ag@TiO_2	0.353 @365 nm, plus 1 @>400 nm	7.5	90	173.6	12
Pt/TiO_2	6.5 @AM1.5	6.5	55	268.8	18
Pt/TiO_2	6 @AM1.5	6	55	460.3	30
Pt/TiO_2	0.37 @350-450 nm	4.62	55	286.0	6
Pt/TiO_2	0.117@350-400nm	4.62	-	492.8	7
Pt/TiO_2	0.15 @UV band	2.77	65	26.1	15
Pt/TiO_2	2 @>420 nm	2	-	20.7	9

Table S2 shows the details of the benchmark research in thermocatalytic H_2 generation from methanol/water mixture (see **Figure 6**). For convenience in comparison, the equivalent solar concentration ratio of a certain reaction temperature was approximately calculated considering a parabolic trough solar collector.

Table S2. Experimental details of the references, related to **Figure 6.**

Material	Reaction temperature(°C)	Approximate intensity (suns)	H_2 generation rate (mL g_{cat}^{-1} h^{-1})	Reference in **Figure 6**
NiO_x/TiO_2	260	54	1202.9	10
$CuO/ZnO/Al_2O_3$	200	45	99.8	38
$CuO/ZnO/Sc_2O_3$	220	49	1452.0	23
Pt/TiO_2	200	45	34.72	4
Ru/TiO_2	300	60	336.0	5
Cu-Zn-Ti oxide	200	45	1133.4	42
$CuO-CeO_2$	300	60	1062.0	35

The effects of solar SPR loading and solar heating

We studied the interaction between the solar concentration and the SPR effect (**Figure S5A**). Pure P25 TiO_2 was selected for the comparison experiment, in which the H_2 production was <5 mL h^{-1} at *C* = 15. With Au SPR loading, the H_2 generation rate increased over 25 times to 110 mL h^{-1}.

In **Figure S5B**, we experimentally compared the H_2 generation with IR band heating (35–65 °C at *C* = 5–9) to that cooled at room temperature (20 °C at *C* = 5–9). At above 65 °C, the H_2 production with IR band heating becomes 2–3 times that with cooling. Through photo-thermal synergy in this work, the energy grade of the IR band is improved to that of solar H_2. The relationship between solar concentration ratio and steady temperature is: *C* = 3 at 35°C, *C* = 5 at 45°C, *C* = 7 at 55°C, *C* = 9 at 65°C, *C* = 12 at 75°C and *C* = 15 at 82°C.

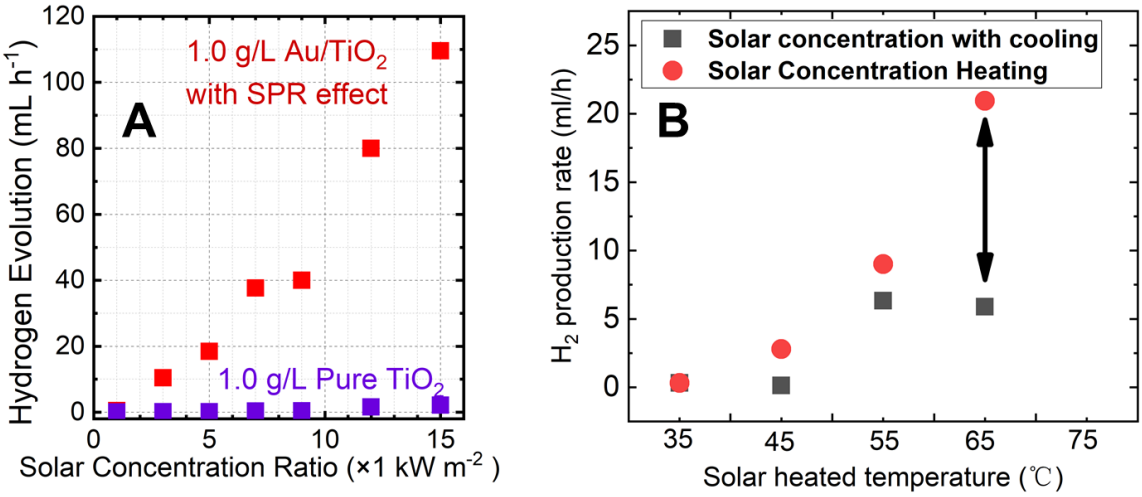

Figure S5. The effects of solar SPR loading and solar heating, related to **Figure 3**. (A) Elevation of H_2 production from SPR Au and photo-thermal effect. (B) The effect of IR band solar heating on H_2 production.

Transient photocurrent

Figure S6 shows the transient photocurrent curve. The transient photocurrent was measured for 1, 5 and 9 suns with light chopping to control the on/off state of incident sunlight. The continuously rising shape of the transient photocurrent was observed for 1, 5 and 9 suns.

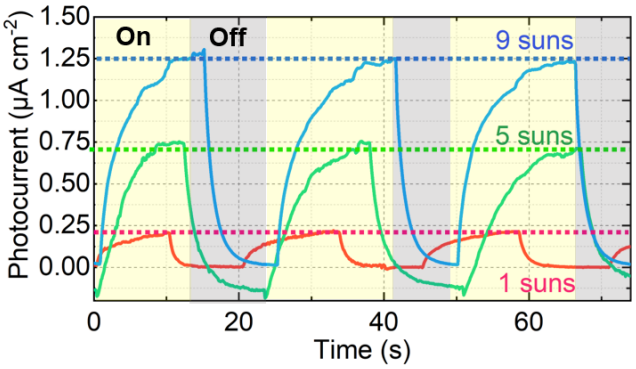

Figure S6. The transient photocurrent curve measured for 1, 5 and 9 suns when the concentrated sunlight is on/off, related to **Figure 4**.

Transmitted solar spectrum energy

In semiconductor-based photocatalysis or photo-thermal catalysis, the unabsorbed and scattered sunlight is transmitted and wasted. In **Figure S7A**, by measuring the transmitted sunlight intensity, for light spot diameter of 3.8 cm, the total input sunlight into the system is 7–21 W. The transmitted sunlight takes a constant proportion in the total sunlight input, which is 20%, 10%, and 5% for 0.1, 0.5, and 1.0 g L^{-1}, respectively. We used a spectrometer to show that the transmitted spectrum consisted of the re-radiated (500 nm), scattered (600 nm), and unabsorbed (700–1100 nm) sunlight by the catalyst (**Figure S7B**). Since the transmitted solar energy takes a considerable percentage and mainly exists in the Vis-NIR band, we chose the mono-silicon PV cell to generate electricity. The bandgap of mono-silicon (1.2–1.3 eV) has a good match with the energy grade of the Vis-NIR band, minimizing the heat relaxation irreversibility.

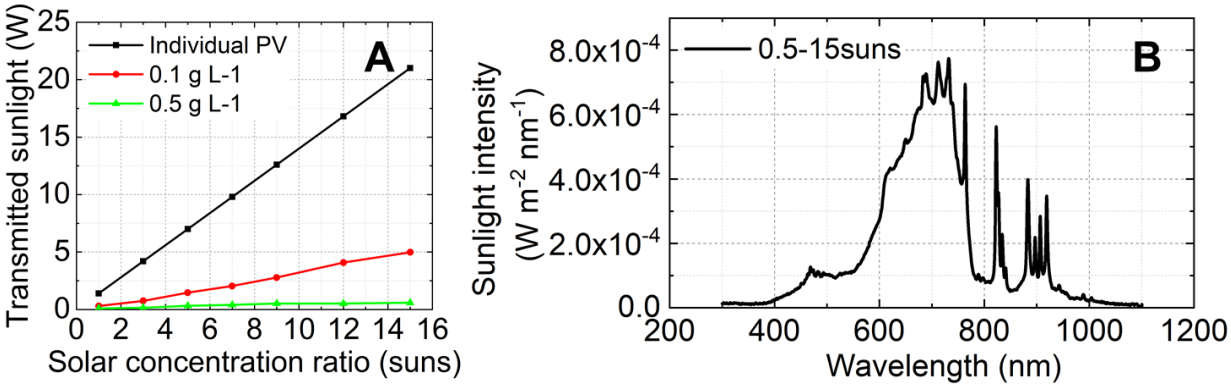

Figure S7. (A) The transmitted sunlight energy from reaction solution of 0.1–1.0 g L^{-1} catalyst concentration. (B) The transmitted spectrum measured at 1.0 g L^{-1} and 15 suns, related to **Figure 7**.

Voltage-current results of the PV cell

Figure S8A–E shows the U-I curve of the PV cell at different catalyst concentrations and sunlight intensity. Moreover, a comparison was also made with an individual PV cell under full-spectrum sunlight.

In **Figure S8F**, the individual PV cell shows a rapid decrease in the current value when the external circuit voltage increases. Such a rapid decrease can result in a lower solar-to-electricity conversion efficiency than the

integrated PV. This indicates that the transmitted spectrum may be most desirable for the mono-silicon PV bandgap.

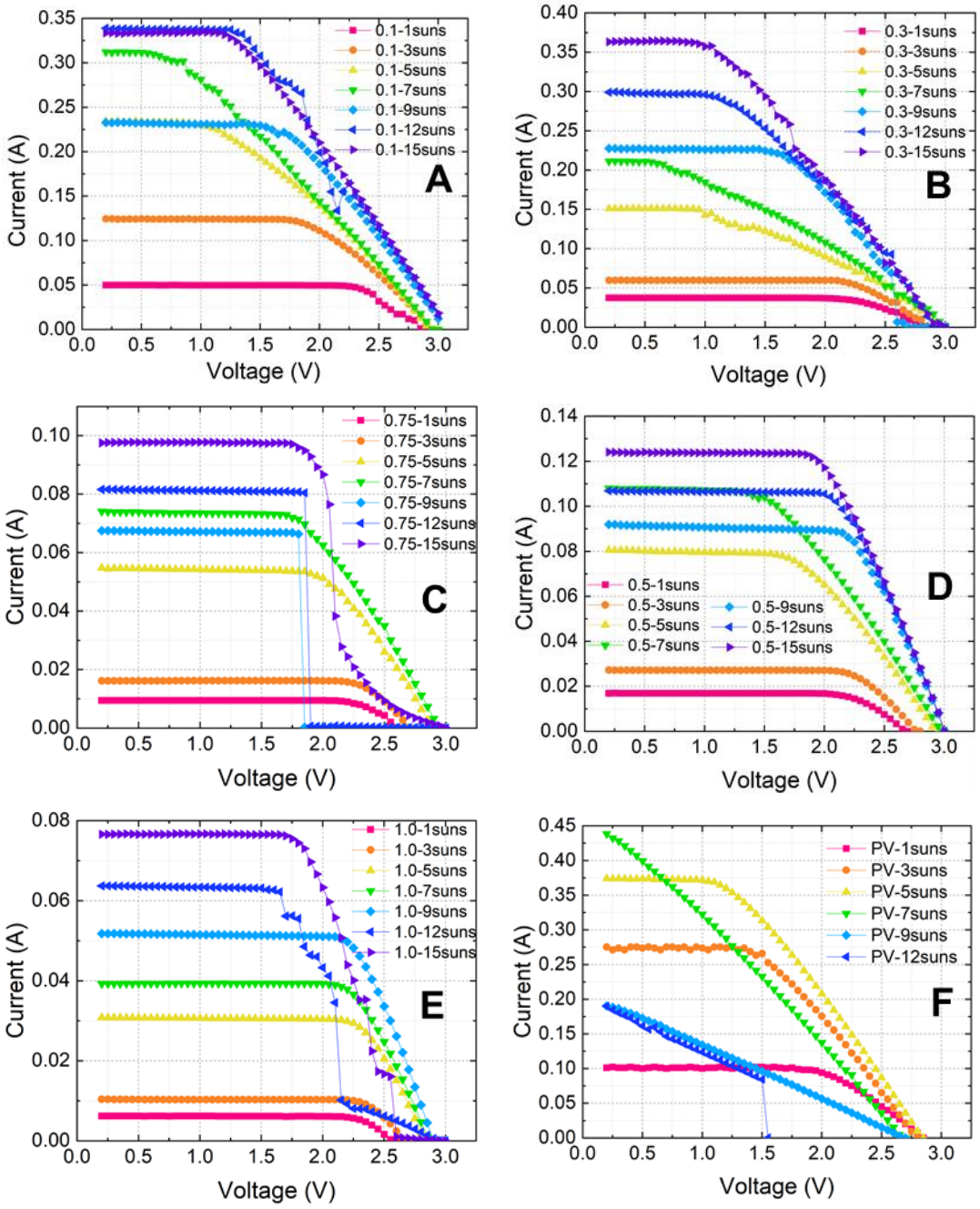

Figure S8. Voltage-current character of the mono-silicon PV cell integrated with (A) reaction system with 0.1 g L^{-1} catalyst (B) reaction system with 0.3 g L^{-1} catalyst (C) reaction system with 0.5 g L^{-1} (D) catalyst reaction system with 0.75 g L^{-1} and (E) catalyst reaction system with 0.3 g L^{-1} catalyst. (F) The voltage current character of an individual PV cell. Related to **Figure 7**.

Energy flow of the individual photo-thermal H_2 and PV generation

We analyzed the energy flow for the individual cases of photovoltaics or 0.5 g L^{-1} photo-thermocatalysis under *C* = 12 (**Figure S9A-B** and **Table S3**). **Figure S9A** shows the energy flow of the individual case of photo-

thermocatalysis. To start with, the input sunlight was concentrated and had an optical loss of 9.75%. In the sunlight absorption process, the photo-thermochemical reaction has a scattering loss of 24.73% and a transmission loss of 17.90%. For the sunlight absorbed by the photo-thermal reaction, the photo effect generates charge carriers (from the UV-Vis band), while the thermal effect generates phonons (from the IR band). Using the extra energy from the UV band, the phonons from the IR band are elevated to solar syngas. The IR phonons not only join the indirect excitation for charge carriers, but also directly activate the adsorbed molecules. In **Figure S9A**, the thermal phonon is depicted to join the UV-Vis band for H_2 production. The photo and thermal effects contribute nearly equally to the H_2 generation process, resulting in H_2 output accounting for 1.21% of the total input sunlight.

Figure S9B shows the energy flow of the individual case of the PV cell. The mono-silicon PV cell has a bandgap suitable for the Vis-NIR band sunlight and may have heat relaxation loss under the full-spectrum input. Moreover, the commercial PV cell is designed for C = 1 and may have a recombination loss at C > 1. Under the concentrated sunlight of C = 12, the combined effect of heat relaxation and recombination in the PV cell leads to an energy loss of 98.10%, with electricity generation accounting for 1.90% of the input sunlight.

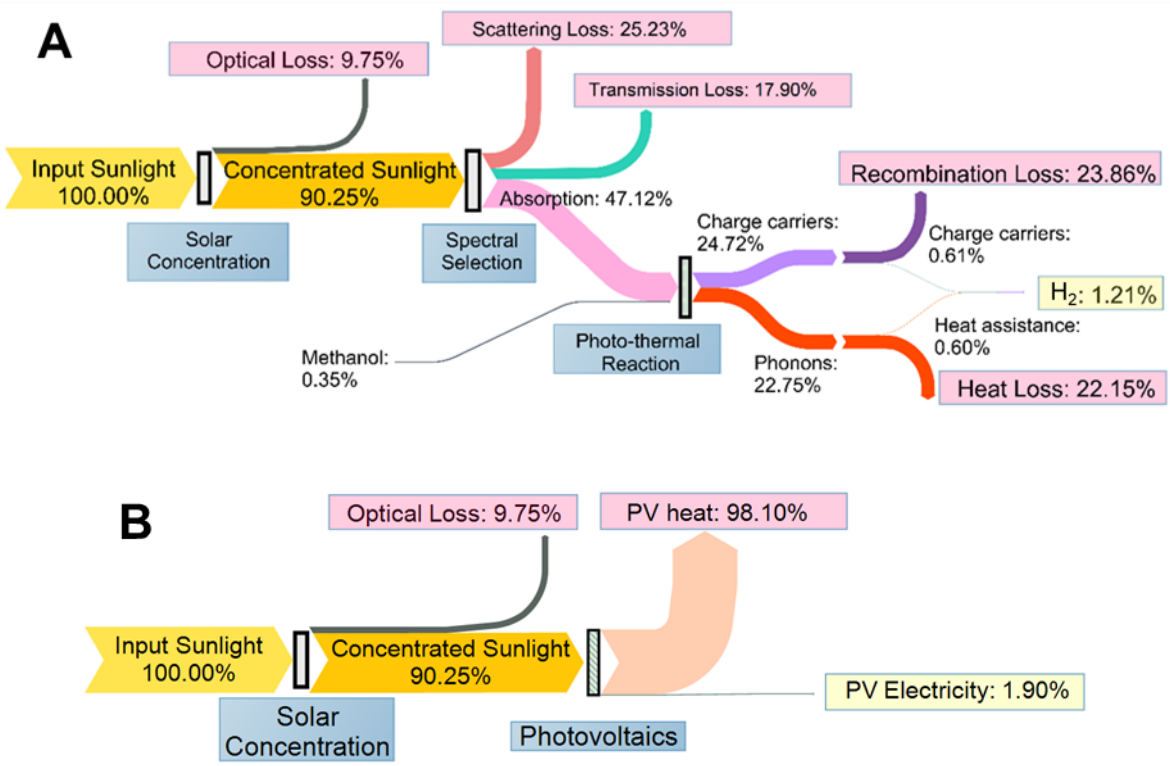

Figure S9. The energy flow chart related to **Figure 9.** (A) Individual case of photo-thermocatalysis and (B) the individual case of PV.

Table S3. Energy loss analysis, related to **Figure 9.**

Terms	Co-production system	Individual photo-thermocatalysis	Individual PV
Input sunlight, *CI*	100%	100%	100%
Input methanol, $\Delta G_{CH_3OH} \cdot n_{CH_3OH}$	0.35%	0.35%	-
Optical loss	9.75%	9.75%	9.75%
Scattering loss, L_{sca}	19.85%	25.23 %	-
Recovered from scattering, R_{sca}	4.88%	-	-
Transmitted sunlight	17.90%	17.90%	90.25%
PV heat, L_{PV}	20.21%	-	88.35%
PV electricity, *P*	2.57%	-	1.9%
Absorbed for H_2 production, $A(\lambda) \cdot CI$	47.62%	47.12%	-
Charge carriers	24.67%	24.37%	-
Phonons/heat	22.95%	22.75%	-
Recombination loss, L_r	23.81%	23.51%	-
Heat loss, L_{heat}	22.10%	22.15%	-
Hydrogen, $\Delta G_{H_2} \cdot n_{H_2}$	1.71%	1.21%	-
Overall conversion efficiency, η_{sys}	4.2%	1.21%	1.9%

Transparent Methods

The experimental apparatus and procedure

Figure S10 shows the experimental apparatus. In **Figure S10A,** the convex lens assembled on the 300 W Xenon lamp (CEL-HXF300, CEAULIGHT) to provide concentrated sunlight. Through controlling the working current and changing the lens and the distance from the reactor to the lamp, the solar concentration ratio is changed at 1–15 suns at the working focus, where the surface of the reaction solution is located. The working focus had a diameter of 60-82 mm for 1-7 suns and a diameter of 40-55 mm for 9-15 suns. **Figure S10B** shows the 82 mm focus for 1 sun and the 55 mm focus for 9 suns. To make comparison on a basis of the same irradiated area but different concentration ratio, the hydrogen generation rate for using a smaller light focus with diameter d_1 was divided by $(d_1/d_2)^2$ before compared with that using a larger focus of diameter d_2. The photos in **Figure S10C** were taken with a filter in front of the camera to avoid overexposure of the picture.

In **Figure S10C**, two types of reactor with inner diameter of d_1 = 82 mm and d_2 = 55 mm is used, to meet the different area of the sunlight focus at different concentration ratios. The reactors were quartz to ensure high sunlight transmittance. Moreover, the side surface of the reactor is coated with a mirrored surface (95% reflectivity) to recover the scattered sunlight. To ensure a same optical thickness of the incident sunlight in the nanofluid, the volume of reaction solution is respectively 100 mL and 50 mL for the two reactors.

Figure S10D shows two square-shaped PV cells fixing on two round-shaped supports. The PV cells are commercially fabricated by connecting in series five Si PV cells with 0.6 V open circuit voltage, thus the rated open circuit voltage is 3.0 V for both PV cells. The areas of the PV cells are respectively 24.5 cm^2 and 15.1 cm^2.

The larger PV cell is integrated with the d_1 = 82 mm reactor, while the smaller one is integrated with the d_2 = 55 mm reactor. Then, both PV cells are connected to a set of aluminum alloy cooling fins to remain near the room temperature during the operation.

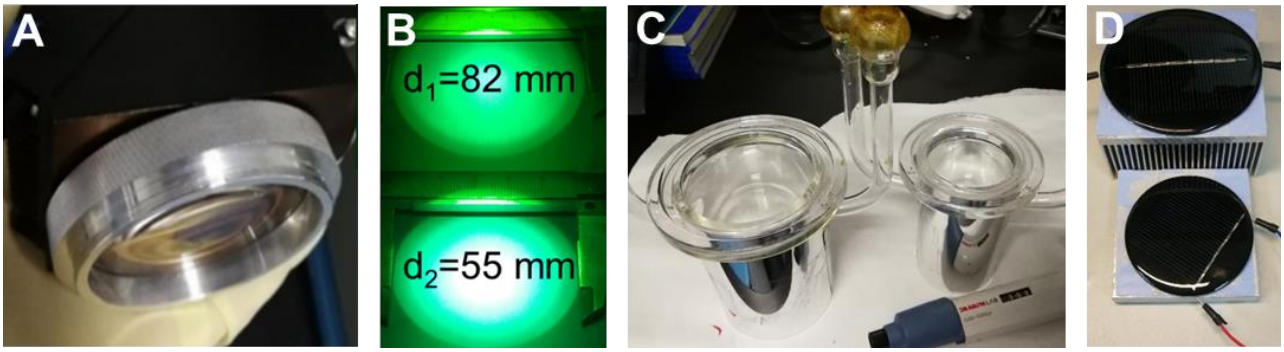

Figure S10. The experimental apparatus related to **Figure 2**. (A) The convex lens on the Xenon lamp. (B) The working focus. (C) The two type of quartz reactors. (D) The photovoltaic cell.

In a typical experiment procedure, the average sunlight intensity on the working focus was measured. As shown in **Figure S11A**, the average sunlight intensity is measured by a five-point average method. The point in the center contributes to 2/3 of the average sunlight intensity, while the average intensity of the other four point on the margin contributes to 1/3 of the average sunlight intensity. The five points are located using a steel plate with a matrix of holes (inset of **Figure S11A**). The sunlight intensity at each point is measured by a light power meter (CEALL- NP2000, CEAULIGHT) with measuring range of 0-20 kW m^{-2}.

After sunlight intensity measurement, a certain volume (100 mL or 50 mL) of the 10 vol% methanol aqueous solution was mixed with Au-TiO_2 catalyst by ultrasonication for 10 min, forming a homogeneous reaction solution with catalyst concentration of 0.1, 0.3, 0.5, 0.75, 1.0 g L^{-1}. Then the reactor was connected to the pipeline (CEL-SPH2N-D, CEAULIGHT, **Figure S11B**) to extract all dissolved gas in it. After the evacuation, N_2 was injected until the absolute pressure is 0.8 atm in the pipeline and reactor. Then the Xenon lamp was turned on wit convex lens for a 9 h continuous experiment. During the experiment, moderate stirring was maintained during the reaction to prevent aggregation. Two water cooling coils at 0 °C were attached to the photo-thermal reactor to condense any evaporated methanol into liquid, which then flew back to the reactor. The pipeline was equipped with circulation and can collect and mix the gaseous product generated during the reaction. Every 30 min, the gaseous product in the pipeline was auto syringed into the GC7920-TFZA gas chromatography to measure the accumulated hydrogen production. The average hydrogen production rate is calculated when the accumulated hydrogen production becomes linear to reaction time.

Figure S11C shows the hybrid system in operation. The inlet concentrated sunlight is partly absorbed by the photo-thermal reaction solution. The upper quartz window is fixed with an electric heating ring (red colored) as a defogger and heated to 115 °C in operation. This prevents the quartz window from being blurred by the steam of water and methanol reactant. The sunlight unabsorbed by Au-TiO_2 (reddish color) is transmitted downward and leaves the reactor bottom for the bottom PV cell.

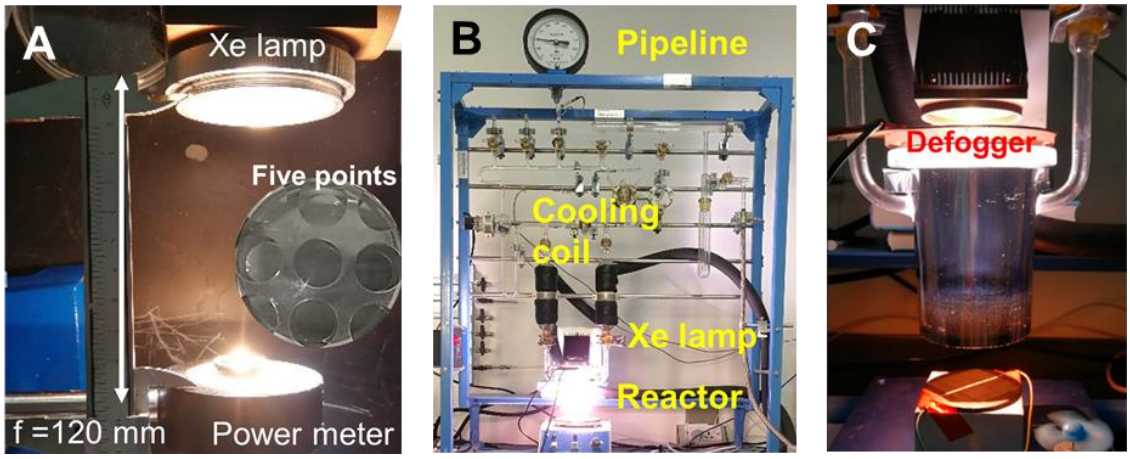

Figure S11. The typical experiment procedure, related to **Figure 2**. (A) Measurement of the average sunlight intensity. (B) Experimental apparatus for the hybrid system under concentrated sunlight. (C) The hybrid system in operation.

Figure S12 shows the preparation of Au-TiO_2 using the deposition-precipitation (DP) method (Sakurai et al., 1993). In the DP method, 1 mol% Au was loaded on Aeroxide P25 TiO_2. In a typical procedure, $HAuCl_4 \cdot 3H_2O$ (0.46 mM, 300 mL) was first added to a three-necked flask and then heated to 80 °C in the oil bath. Then, NaOH (0.1 M) was added to the solution and the pH was adjusted to 7.5. Next, 1 g of TiO_2 was added, and the mixture was stirred at 700 rpm for 3 h. The resultant Au-TiO_2 products were separated and collected with centrifugation, followed by washing with deionized water three times to remove extra Cl^-. The obtained lavender paste was dried in a vacuum oven at the ambient temperature for 24 h and ground to powder.

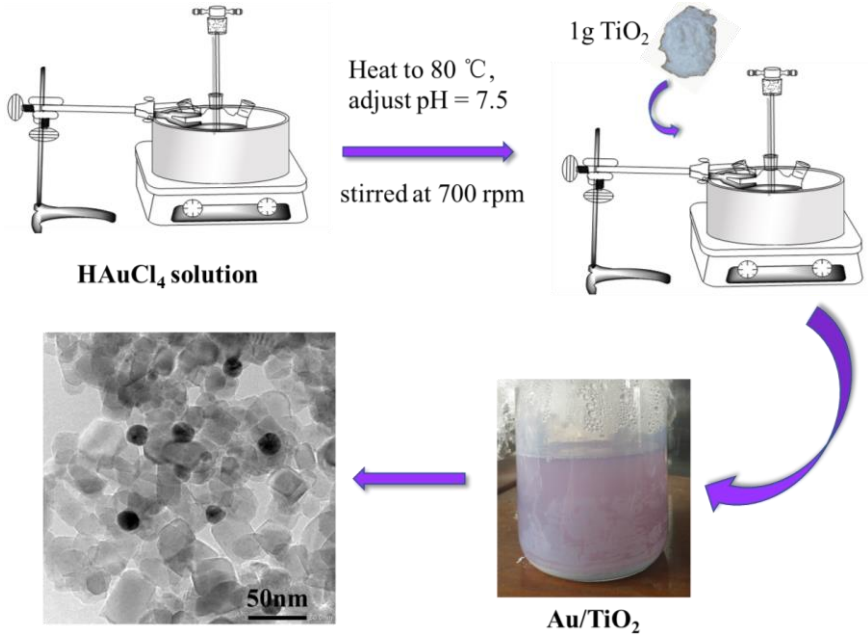

Figure S12. Preparation of Au-TiO_2 photo-thermal catalyst using the deposition-precipitation (DP) method, related to **Figure 2**.

Photocurrent measurement

Figure S13A shows the Au-TiO_2 was fixed on 1 cm × 2 cm indium tin oxide (ITO) coated glass electrodes. The ITO coating has a sheet electrical resistance of 15 Ω/sq. For a typical test, 20 mg of Au-TiO_2 was dispersed homogeneously in 2 mL of 5 wt % Nafion aqueous solution. After 30 mins of ultrasonication, 3-5 drop of the suspension was spin-coated on a piece of ITO glass and put in a vacuum drying oven at ambient temperature for 24 h. To test the stability, the Au-TiO_2 coated electrode was immersed in the electrolyte solution for 24 h and found to remain stable.

Figure S13B-C shows the photocurrent test apparatus. The solar concentration of the Xenon lamp in **Figure S13B** was changed at *C* = 1-9 suns. The sunlight intensity at the electrode position is tested with a CEALL light power meter with measuring range of 0-20 kW m^{-2}. The sensor of the power meter is placed 12.5 cm away from the Xenon lamp, which was the same location of the electrode in photocurrent test. A 2 cm thickness layer of the electrolyte (0.5 M Na_2SO_4 aqueous solution) was placed in front of the power meter sensor as the influence of sunlight attenuation of the electrolyte solution (the inset of **Figure S13B**).

Figure S13C shows the three-electrode system used for the measurement. Considering the neutral PH value of the catalytic solution, the electrolyte was selected as a 0.5 M Na_2SO_4 aqueous solution (Si et al., 2018). The front side of the Au-TiO_2/ITO working electrode was illuminated, and the area of the working electrode dipped in the electrolyte solution was 1 cm^2. The counter electrode was Pt and the reference electrode were Ag/AgCl. All the electrodes were linked to a CHI660e electrochemical workstation. To avoid the influence of the electrolyte temperature, a jacket photoelectrochemical cell with a circulating water bath was used for the measurement. The temperature of the solution was controlled the same as that in photo-thermal hydrogen generation experiments.

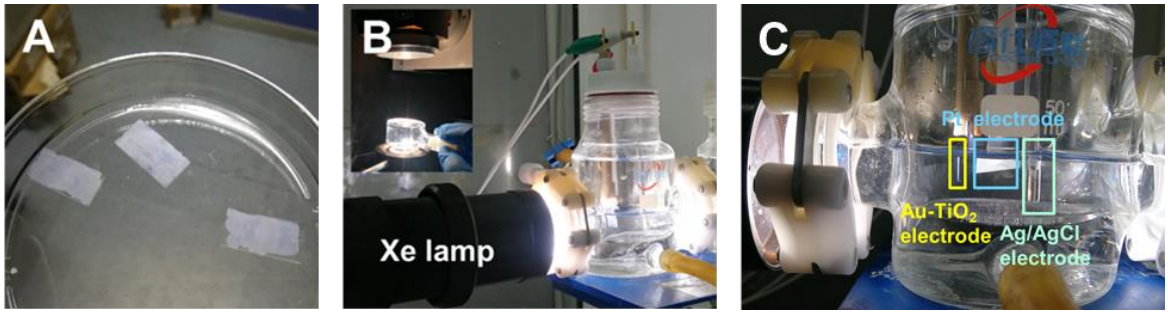

Figure S13. The photocurrent test related to **Figure 4**. (A) The test apparatus. (B) The measurement of simulated sunlight intensity from the Xenon lamp. (C) The three-electrode system.

Voltage-current measurement methods of the PV cell

The voltage-current curve of the PV cell was monitored using a voltammetry measuring method. The measuring mechanism is shown in **Figure S14A**. The voltage-current measurements were made using an DC electronic load (IT8510, ITech), where the inner resistance R_{Adjust} was programmed to sweep the output voltage at 0.2–3.0 V at a sweep rate of 50 mV s^{-1}. The voltage was collected by the inset voltmeter of the DC electronic load (0–18 V, precision: 0.025%+0.025%FS) and the current was collected by an external high precision ammeter (0–500 mA, precision: 0.08%FS). For each set of solar concentration ratio and catalyst concentration, the apparatus scans the voltage from approximately the short-circuit state (0.2 V) to the open-circuit state (3.0 V)

for the voltage-current curve of the PV cell. After the voltage scan, the maximum power point can be found as the maximum of the product of voltage and current.

The experimental setup is shown in **Figure S14B**. The blue reading on the top is from the high precision ammeter, while the green reading on the left at the bottom is from the voltmeter. The readings were collected and depicted into voltage-current curves. In addition to the voltammetry measurement, a 1 W electric fan (blue color) and a 24×0.05 W LED array were used as examples of appliances. The continuous operation of the appliances is shown in **Video S2** and **S3**.

Figure S14C shows the measurement of average sunlight intensity transmitted downward from the reactor bottom. Before each set of PV voltage-current measurement, the transmitted sunlight intensity is measured by the five-point average method same as that used for measuring the average sunlight intensity at the focus. The sunlight intensity at each point is measured by the light power meter with measuring range of 0-20 kW m^{-2}.

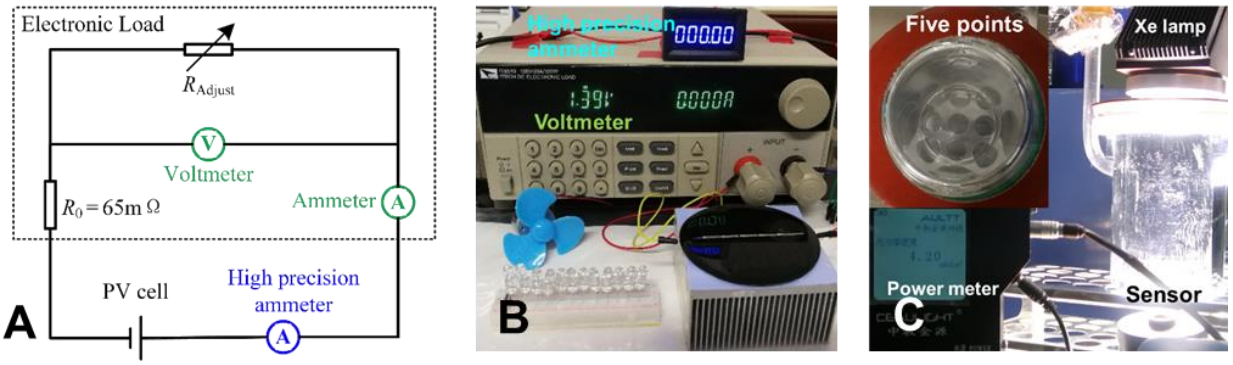

Figure S14. The voltage-current measurement related to **Figure 7.** (A) Measurement circuit. (B) The real setup of the measurement circuit. (C) The measurement of the transmitted sunlight intensity.

Energy flow analysis methods

We analyzed the energy flow at full spectrum to explain the reduction in energy loss through cascading utilization. For the upstream solar concentration and spectrum selecting processes, the energy balance is

$$CI = A(\lambda)\cdot CI + (Q_{trn} + R_{sca}) + (1 - T_{lens}(\lambda))\cdot CI + L_{sca} \quad \text{(S1)}$$

In Eq. S1, the input is the full-spectrum concentrated sunlight *CI* and methanol consumption $\Delta G_{CH4O}\cdot n_{CH4O}$. The amount of the energy in methanol is shown as percentage of the input sunlight. In the spectrum selection process, the photo-thermal reaction system absorbs the narrow-band sunlight $A(\lambda)\cdot CI$ while transmitting the other band Q_{trn} for PV. The optical loss, $(1 - T_{lens}(\lambda))\cdot CI$, occurs at the concentrator lens and the quartz window of the reactor. The scattering occurs on the Au-TiO_2 nanoparticles with some recovered by the reflective film as R_{sca}. All the terms in Eq. S1 can be measured experimentally, and then the scattering loss L_{sca} can be calculated.

For the downstream photo-thermocatalysis and photovoltaic processes, the energy balance is expressed as follows.

$$A(\lambda)\cdot CI + \Delta G_{CH4O}\cdot n_{CH4O} = L_r + L_{heat} + \Delta G_{H2}\cdot V_{H2}/22.4 \quad \text{(S2)}$$

$$R_{\text{sca}} + Q_{\text{trn}} = L_{\text{PV}} + P \quad \text{(S3)}$$

In Eq. S2, the output of the system includes H_2 and PV electricity. Under the absorbed spectrum energy $A(\lambda)\cdot CI$, the photo-thermal reaction generated solar H_2 with chemical energy of $\Delta G_{\text{H2}} \cdot V_{\text{H2}} / 22.4$, plus a recombination loss of L_r. The total input of the PV cell is the sum of the transmitted sunlight Q_{trn} and the recovered scattered sunlight R_{sca}. The corresponding PV electricity output is P, with the energy loss from PV recombination and Ohmic loss as L_{PV}.

Calculation process of individual photo-thermal efficiency

We chose the highest H_2 generation rate at each solar concentration ratio to calculate the efficiency of individual photo-thermal hydrogen production. For example, the 1.0 g L^{-1} has the highest H_2 generation rate among different mass concentrations under C = 12. According to Eq.1, after eliminating the output of PV electricity in the nominator, we have the efficiency for H_2 production

$$\eta_{\text{ptc}} = \frac{\Delta G_{\text{H}_2} \cdot V_{\text{H}_2} / 22.4}{C \cdot \int_{300\text{ nm}}^{2500\text{ nm}} I(\lambda) d\lambda + \Delta G_{\text{CH}_3\text{OH}} \cdot n_{\text{CH}_3\text{OH}}} . \quad \text{(S4)}$$

In the denominator, the Gibbs energy for H_2 is ΔG_{H_2} =237.129 J $mmol^{-1}$ and V_{H_2} is the volume of H_2 (79.9 mL, considered at standard condition) as shown in Figure 5A.

In the nominator, the C is the solar concentration ratio. The incident solar energy is calculated by

$$C \cdot \int_{300\text{ nm}}^{2500\text{ nm}} I(\lambda) d\lambda = C \cdot 3600 \times A \cdot \int_{300\text{ nm}}^{2500\text{ nm}} flux(\lambda) d\lambda$$

Where the A is the irradiated area of a 45 mm diameter round-shape focus. The total solar energy flux $C \cdot \int_{300\text{ nm}}^{2500\text{ nm}} flux(\lambda) d\lambda$ is the solar power flux at the focus. In this case, the $\int_{300\text{ nm}}^{2500\text{ nm}} flux(\lambda) d\lambda$ is 12000 W m^{-2}.

The consumed molar amount of methanol $n_{\text{CH}_3\text{OH}}$ is considered $0.33 n_{\text{H}_2}$ according to the 1:3 stoichiometric ratio to H_2 in methanol reforming, though the consumption of methanol can be much lower in photo-thermal catalysis (Fang et al., 2019). The $\Delta G_{\text{CH}_3\text{OH}}$ here is 726 J $mmol^{-1}$ considering the Gibbs free energy change in methanol combustion reaction.

With all the above, the calculation goes as

$$\eta_{\text{ptc}} = \frac{79.9 \times 237.129 / 22.4}{12000 \times 3600 \times (0.045/2)^2 \times \pi + 726 \times 0.33 \times 79.9 / 22.4} \times 100\% = 1.21\%$$

Supplemental References

Fang, S., Sun, Z. & Hu, Y. H. (2019). Insights into the Thermo-Photo Catalytic Production of Hydrogen from Water on a Low-Cost NiOx-Loaded TiO2 Catalyst. ACS Catal. 9, 5047-5056.

Sakurai, H., Tsubota, S. & Haruta, M. (1993). Hydrogenation of CO2 over Gold Supported on Metal Oxides. Appl. Catal. A Gen. 102, 125-136.

Si, Y., Cao, S., Wu, Z., Ji, Y., Mi, Y., Wu, X., Liu, X. & Piao, L. (2018). What is the predominant electron transfer process for Au NRs/TiO2 nanodumbbell heterostructure under sunlight irradiation? Appl. Catal. B: Environ. 220, 471-476.

Vincenzi, D., Busato, A., Stefancich, M. & Martinelli, G. (2010). Concentrating PV system based on spectral separation of solar radiation. Physica Status Solidi 206, 4.